Monte-Carlo Simulations of Electron Capture Branching Ratio Measurements for the TITAN Facility

by

Shakil Seeraji

B.Sc. (Hons.), Military Institute of Science and Technology, 2010

Thesis Submitted in Partial Fulfillment
of the Requirements for the Degree of

Master of Science

in the
Department of Chemistry
Faculty of Sciences

SIMON FRASER UNIVERSITY
January 2015

APPROVAL

Name:	Shakil Seeraji
Degree:	Master of Science
Title of Thesis:	Monte-Carlo Simulations of Electron Capture Branching Ratio Measurements for the TITAN Facility
Examining Committee:	Dr. .... Chair
	Dr. Corina Andreoiu, Associate Professor, Senior Supervisor
	Dr. Jens Dilling, Professor, Supervisor
	Dr. Krzysztof Starosta, Associate Professor, Supervisor
Date Approved:	January, 2015

Partial Copyright Licence

The author, whose copyright is declared on the title page of this work, has granted to Simon Fraser University the non-exclusive, royalty-free right to include a digital copy of this thesis, project or extended essay[s] and associated supplemental files ("Work") (title[s] below) in Summit, the Institutional Research Repository at SFU. SFU may also make copies of the Work for purposes of a scholarly or research nature; for users of the SFU Library; or in response to a request from another library, or educational institution, on SFU's own behalf or for one of its users. Distribution may be in any form.

The author has further agreed that SFU may keep more than one copy of the Work for purposes of back-up and security; and that SFU may, without changing the content, translate, if technically possible, the Work to any medium or format for the purpose of preserving the Work and facilitating the exercise of SFU's rights under this licence.

It is understood that copying, publication, or public performance of the Work for commercial purposes shall not be allowed without the author's written permission.

While granting the above uses to SFU, the author retains copyright ownership and moral rights in the Work, and may deal with the copyright in the Work in any way consistent with the terms of this licence, including the right to change the Work for subsequent purposes, including editing and publishing the Work in whole or in part, and licensing the content to other parties as the author may desire.

The author represents and warrants that he/she has the right to grant the rights contained in this licence and that the Work does not, to the best of the author's knowledge, infringe upon anyone's copyright. The author has obtained written copyright permission, where required, for the use of any third-party copyrighted material contained in the Work. The author represents and warrants that the Work is his/her own original work and that he/she has not previously assigned or relinquished the rights conferred in this licence.

Simon Fraser University Library
Burnaby, British Columbia, Canada

revised Fall 2013

Abstract

A novel technique has been developed to measure the electron capture branching ratios (ECBRs) of key intermediate nuclei involved in double-β decay using the TITAN facility, TRIUMF's Ion Trap for Atomic and Nuclear Science Facility.

Knowledge of ECBRs is essential to evaluate the nuclear matrix elements of double-β decay for both two-neutrino double-β decay ($2\nu\beta\beta$) and neutrino-less double-β decay ($0\nu\beta\beta$) processes. In most of the cases of interest the ECBRs are poorly known or completely unknown because the EC process is suppressed by several orders of magnitude relative to their β-decay counterpart due to energy consideration. In addition, traditional methods of measuring these ratios suffer from large backgrounds due to the many orders of magnitude more intense β-decay.

A new method for measuring EC branching ratios was implemented by using the TITAN ion trap at the TRIUMF ISAC (Isotope Separator and Accelerator) radioactive beam facility. In these experiments the Electron Beam Ion Trap (EBIT) is used as a spectroscopy Penning trap, where the electrons from β-decay will be confined by trap's magnetic field and transported out of the trap, while the x-rays from EC are detected by Si(Li) x-ray detectors that are radially installed around the trap through seven open ports towards the trap's center.

A comprehensive GEANT4 based Monte-Carlo simulation has been developed to optimize the TITAN-EC experimental set-up and measurements at TRIUMF as analytical tool. The developments, evolution and validation of this Monte-Carlo simulation tool are described in this thesis.

Keywords: Detectors, ECBR, HPGe, GEANT4, Monte-Carlo, Radioactive Beam, Simulations, Si(Li), TITAN-EC, Traps, TRIUMF

Acknowledgments

I would like to express my deepest gratitude to my senior supervisor Dr. Corina Andreoiu, for her excellent guidance, caring, patience, and providing me with an excellent atmosphere for doing research. I am truly grateful for the opportunities that I have been given in the Nuclear Science Group. I would also like to thank my supervisory committee, Dr. Jens Dilling and Dr. Krzysztof Starosta for their guidance and suggestions throughout the masters program. And especial thanks to Dr. Kyle Leach for supporting and guiding me with many aspects of this thesis. Also I would like to thank my colleagues at the SFU Nuclear Science Lab and TITAN group members for their help and suggestions.

Finally I would like to thank my wife, family and friends, who supports me throughout my graduate studies.

Contents

List of Tables

List of Figures

Chapter 1

Introduction and Theoretical Aspects

The TITAN-EC project has developed a unique in-trap decay spectroscopy facility to measure electron capture branching ratios (ECBRs) of short lived intermediate nuclides involved in double-beta (β) decay at the ISAC radioactive isotope facility at TRIUMF (Canada's National Laboratory for Particle and Nuclear Physics) located in Vancouver, Canada. It facilitates the TRIUMF's Ion Traps for Atomic and Nuclear science (TITAN) and the Electron Beam Ion Trap (EBIT) to enable in-trap x-ray and gamma (γ)-ray spectroscopy on radioactive isotopes stored in the center of the spectroscopy ion trap.

The ECBR information is important for determination of nuclear matrix elements (NME) of double-β decay for both two-neutrino double-β decay ($2\nu\beta\beta$) and neutrino-less double-β decay ($0\nu\beta\beta$) processes. In most cases the ECBRs are poorly known or unknown because the measurements are performed with conventional methods. In the conventional EC/β branching ratios measurement technique, a radioactive sample is implanted into a movable tape and then moved towards one or several x-ray and β detectors. Major concerns and limiting factors in these experiments are beam/target contaminants, x-ray absorption in the carrier material and detection of the electron capture (EC) process which is suppressed by the high backgrounds induced by intensely dominating β^- decays. To overcome these problems, in-trap x-ray and γ-ray spectroscopy are performed using the unique ion trap facility of TITAN, where produced radioactive ions from the ISAC facility are injected and stored in backing free environment, i.e., without implanting in any medium to observe their decays. In these experiments, the EBIT is used as a spectroscopy trap, where the electrons from β^--decays are confined by the strong 6 T magnetic field, and the x-rays from EC are detected by an array of lithium drifted silicon (Si(Li)) x-ray detectors. These detectors are radially installed around the trap through seven ports opening towards the trap's center.

TITAN-EC program proposed to measure the ECBR of seven different important cases. Table 1.1 shows the list of proposed odd-odd intermediate nuclei that will be investigated by the TITAN-EC experiment. In all of these, the daughter isotopes are double-β decay candidates, which are presently under intense experimental investigations at different facilities [1].

Table 1.1: List of proposed odd-odd intermediate nuclei that will be investigated by the TITAN-EC experiment [1].

Mother Nucleus	Transition	Daughter nucleus	$K_\alpha[keV]$	$T_{1/2}$
^{100}Tc	$1^+ \rightarrow 1^+$	^{100}Mo	17.5	15.8 s
^{110}Ag	$1^+ \rightarrow 1^+$	^{110}Pd	21.2	24.6 s
^{114}In	$1^+ \rightarrow 1^+$	^{114}Cd	25.3	71.9 s
^{116}In	$1^+ \rightarrow 1^+$	^{116}Cd	21.7	14.1 s
^{82m}Br	$2^- \rightarrow 1^+$	^{82}Se	11.2	6.1 min
^{128}I	$1^+ \rightarrow 1^+$	^{128}Te	27.5	25.0 min
^{76}As	$2^- \rightarrow 1^+$	^{76}Ge	9.9	26.2 hr

The double-β decay involves contributions from all 1^+ states, with the 1^+ ground state in the intermediate nuclei having the most important contribution to the $2\nu\beta\beta$ decay rate [2]. This hypothesis is known as the single-state dominance (SSD) hypothesis. Among the double-β candidates to be studied in this program in which this situation is likely to occur are the ^{100}Mo, ^{110}Pd, ^{116}Cd, and ^{128}Te nuclei. The ground-state transitions contribution to the NME can be calculated and improved by measuring the single β^+/EC and β^--decay rates.

This chapter provides a brief introduction to the theoretical aspects of the physics involved in the TITAN-EC project, followed by the working principle of the semiconductor detectors. Chapter 2 presents the radioactive beam production at TRIUMF, followed by the TITAN and TITAN-EC experimental setup. The spectroscopy EBIT trap, TITAN-EC array (array of Si(Li) detectors), high-purity germanium (HPGe) detector system and related electronics are also introduced in this chapter. In chapter 3, a detailed introduction of GEANT4 software package is given, followed by TITAN-EC's simulation processes in GEANT4. In the simulation process discussion, the development of TITAN-EC's geometry in GEANT4 is examined, followed by demonstration of simulations generating the prediction for the photopeak detection efficiency of the TITAN-EC array as well as detectors performance at a wide range of experimental conditions, and the impact of different shielding on background. In addition, the performance of the HPGe detector is compared with the TITAN-EC array to evaluate the experimental capability with a range of isotopes for the future development of the project. Chapter 4 focuses on the obtained simulation results, systematically comparing these results with experimental data to verify the accuracy and demonstrate the significance of simulations for ECBR measurements using ion traps. In chapter 5, the development and operating principle of an annealing station dedicated for maintaining and refurbishing the HPGe detectors that would be used within this program is presented. The conclusions and future directions for the validated TITAN-EC simulations are presented in chapter 6.

1.1 Electron Capture Decay

The electron capture (EC) decay process is unique among the decays, since this process requires nuclear interaction with an orbital electron [3]. The possibility of EC was first suggested by Yukawa and Sakata in 1935 and 1936, respectively [4] and described by Nobel Laureate Luis Alvarez in 1938 [5]. In EC, one of the protons in the parent nucleus captures an orbital electron to become a neutron and then emits a neutrino, conserving mass and energy. The reaction can be written as:

$$^{A}_{Z}X + e_i^- \rightarrow ^{A}_{Z-1} Y_{N+1} + \nu_e \qquad\qquad p + e^- \rightarrow n + \nu_e \tag{1.1}$$

In these reactions one lepton is on each side of the reaction equation, so lepton number is conserved along with nucleon number [4]. The decay energy of the EC from the i^{th} shell is:

$$E_i = [m_X + m_e - m_Y]c^2 - W_i \tag{1.2}$$

where m_X and m_Y are the nuclear mass of parent and daughter nucleus, respectively, m_e is the mass of electron and W_i is the binding energy of i^{th} shell electrons in the parent atom. Since, the binding energy differences of electrons in the atom can be neglected, Eq. 1.2 can be converted to atomic masses to yield

$$E_i = [M_X - M_Y]c^2 - W_i \tag{1.3}$$

where M_X and M_Y are the atomic masses of parent and daughter atom, respectively. The condition for EC to occur is:

$$M_X(Z,A) - M_Y(Z-1,A) > W_i/c^2 \tag{1.4}$$

Electron capture mainly occurs in high-Z nuclides [3], where nuclear radii are larger and electronic orbits are more compact [6]. Normally electrons are captured from the innermost electrons shell since they are closest to the nucleus and have the maximum overlap of the wave function at the center of the nucleus. K-shell has the closest electron to nucleus, so most likely electron capture occurs with a K-shell electron; a process that is called K capture. Similarly, electron capture from L (L capture) and M (M capture) is also possible, but less probable. As electron capture has occurred, there will be one electron short in one of the orbital shells and the daughter is typically created with an electron in an excited state. To get back to ground state, electrons from higher levels will successively cascade downwards to fill the vacancy and emit x-rays with specific energies known as characteristic x-rays [3]. Figure 1.1 shows a K-shell vacancy created by electron capture being filled by a L-shell electron followed by the emission of characteristic x-ray.

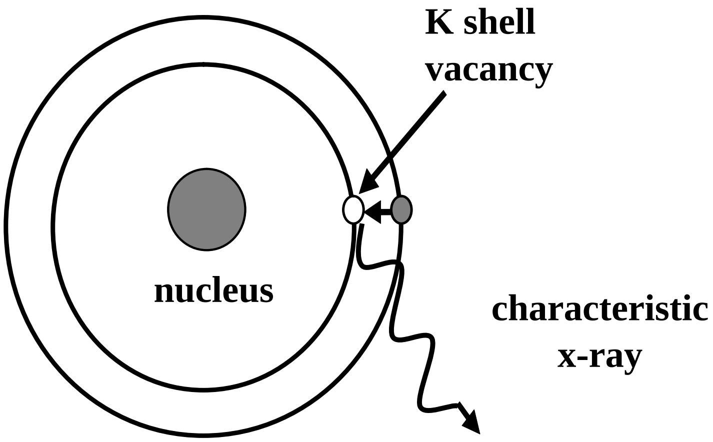

Figure 1.1: The EC process showing a K-shell vacancy created by capturing an electron by nucleus. The vacancy is filled by an L-shell electron followed by emission of characteristic x-ray.

The energies of the x-rays emitted are equivalent to the subshells that mark the beginning and end of the electronic transitions. The most commonly observed transition is $K_{\alpha 1}$, which corresponds to an electric transition from L_3 subshell to K-shell to fill the electron vacancy. Similarly, $K_{\alpha 2}$ is the

$L_2 \rightarrow K$ electronic transition, $K_{\alpha 3}$ is the $L_1 \rightarrow K$ transition and K_β represents combinations of all transitions from M-shell to K shell. Table 1.2 shows characteristic x-ray labels based on the shell transition.

Table 1.2: Characteristic x-ray nomenclature

Transition	x-ray Nomenclature
$L \rightarrow K$	K_α
$M \rightarrow K$	K_β
$M \rightarrow L$	L_α
$N \rightarrow L$	L_β

For the TITAN-EC project these transitions are essential to extract the information about ground state properties of nuclear wave functions which are an important ingredient and a benchmark of theoretical calculations for the nuclear transition matrix element [7].

Seven specially designed 5 mm thick lithium drifted silicon (Si(Li)) detectors are used in the TITAN-EC experimental setup to observe x-rays following EC the process. Details of this process will be explained in the subsequent chapters.

1.2 Double-β Decay

Double-beta (β) decay [8] is a two-step weak interaction process. In this process, the mass A of the parent and daughter nuclei stays constant while the proton number, Z changes by two units. The Weizsacker mass formula [9] illustrates the condition for the appearance of double-β decays; this formula also determines the Z dependence of nuclear mass and whether a nucleus close to stability is stable or will undergo β decay [10]. Here, the mass of the atom with Z protons and $(A-Z)$ neutrons is given by:

$$M(Z,A) = ZM_H + (A-Z)M_n - a_v A + a_s A^{2/3} + a_{sym}\frac{(A/2-Z)^2}{A} + a_{Coul}\frac{Z^2}{A^{1/3}} + \delta_p \qquad (1.5)$$

where M_H is the mass of a Hydrogen atom, M_n is the neutron mass, the volume term coefficient is a_v= 15.69 MeV, the surface term coefficient is a_s = 17 MeV, the symmetry energy coefficient is a_{sym}

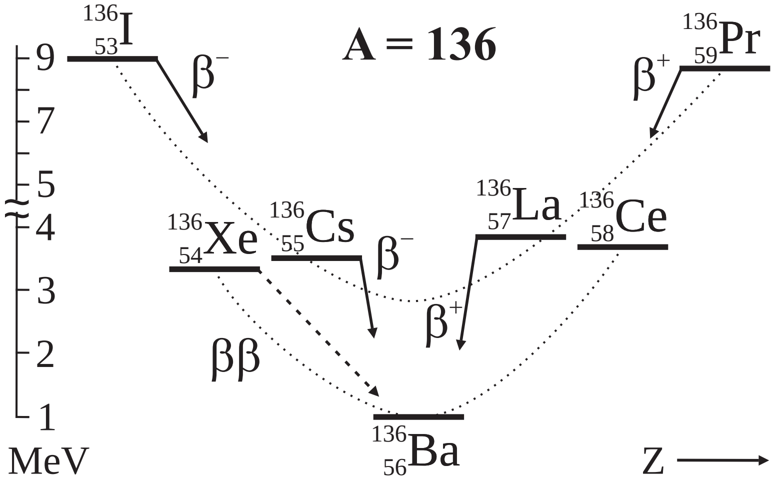

Figure 1.2: Two parabolas for even-$A = 136$ isobars. Normal β decay is either forbidden or strongly suppressed for the nuclei ^{136}Ce and ^{136}Xe. However, double-β decay to the daughter isotope ^{136}Ba is possible. (Reprinted with permission from Ref. [10].)

= 93.15 MeV, the Coulomb energy coefficient is a_{Coul} = 0.714 MeV [11]. Experimentally it has been found that even-even nuclei are more stable than odd-even or odd-odd nuclei. For this reason the pairing term has three different values, shown in Table 1.3, and pairing term values are taken from Ref. [11].

Table 1.3: Experimentally determined values for the pairing term δ_p in the Weizsacker mass formula

Description	δ_p
even-even nuclei	$\frac{-12}{A^{1/2}}$ MeV
even-odd and odd-even nuclei	0
odd-odd nuclei	$\frac{+12}{A^{1/2}}$ MeV

For isobars with odd-A, the pairing term vanishes in Eq. 1.5 and mass $M_A(Z,A)$ is described by a parabola with typically only one stable isotope for a given A. For the case of even-A, two parabolas exist shifted by pairing term value ($\pm\delta_P$) from the odd-A parabola. Two parabolas for even-$A = 136$ are displayed in Figure 1.2 [10].

Double-β decay takes place in cases where single β decay is either energetically forbidden when

$$M_A(Z,A) > M_A(Z+2,A) \quad \textit{and} \quad M_A(Z,A) < M_A(Z+1,A) \tag{1.6}$$

or strongly suppressed by a large spin difference of the involved nuclear state [10].

According to the Fermi theory of β-decay, we can use the decay constant λ to lead us to the expression for the partial half life, $t_{1/2}$. Knowing that $\lambda = \frac{ln(2)}{t_{1/2}}$, it leads to

$$ft = \frac{2\pi^3\hbar^7 ln(2)}{g^2 {m_e}^5 c^4 |M_{if}|^2} \tag{1.7}$$

where f is the phase space integral, which is a dimensionless quantity that depends only on the charge Z of the daughter nucleus and the average decay energy, Q. M_{if} is the nuclear matrix element which describes the transition probability of the nucleus from initial to final states, g is the strength constant for weak interaction and c is the speed of light. The phase space integral can be roughly approximated by:

$$f \approx \frac{1}{30}\left(\frac{Q}{m_e c^2}\right)^5 \tag{1.8}$$

The quantity on the left side of Eq. 1.7 is called ft-value, which provides a way to compare the β-decay probabilities in different nuclei. The β-decay $log(ft)$ values depend heavily on the transition Q value. Equation 1.8 indicates that the phase space integral scales roughly as the Q value to the 5^{th} power. As a result, decays which have a larger phase space factor are heavily favored. Figure 1.3 shows the energy requirement for double-β decay. This process is one of the rarest known radioactive decay, and it is predicted in only 36 isotopes [12]. The rate of the process is characterized by its very long lifetime (more than 10^{18} years). Double-β decays are expected to happen in at least two modes: the two-neutrino double-β ($2\nu\beta\beta$) and the neutrino-less double-β ($0\nu\beta\beta$) decays. Both cases are explained in the following sections.

1.2.1 2ν and 0ν Double-β Decay

Double-β decay ($2\nu\beta\beta$) is a process in which two β decays occur simultaneously with emission of two electrons and antineutrinos. Goeppert-Mayer first suggested $2\nu\beta\beta$ in 1935 [8] with the process

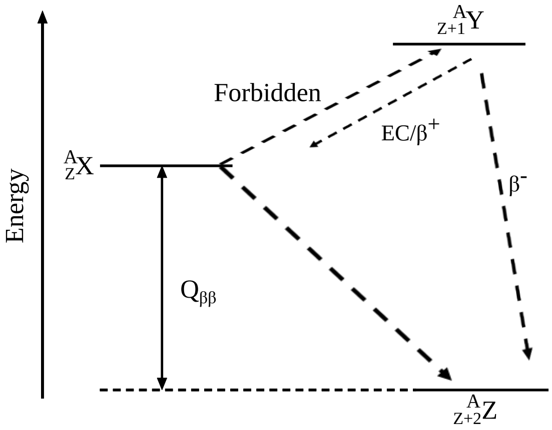

Figure 1.3: A schematic diagram demonstrating the energy requirements for double-β decay. A parent nucleus ${}^{A}_{Z}X$ decays to a daughter nucleus ${}^{A}_{Z+2}Z$ because the intermediate single β decay to ${}^{A}_{Z+1}Y$ is energetically forbidden.

$$(Z,A) \rightarrow (Z+2,A) + 2e^{-} + 2\overline{\nu_e} \tag{1.9}$$

As mentioned earlier, this decay occurs only if the initial nucleus is less bound than the final one, but both must be more bound than the intermediate one. This condition is fulfilled only by some even-even nuclei. The nuclear transition energy ($Q_{\beta\beta}$) for this process is defined as

$$Q_{\beta\beta} = m(A,Z) - m(A,Z+2) - 2m_e \tag{1.10}$$

where $m(A,Z)$ and $m(A,Z+2)$ are the masses of the initial and final nuclei. This decay involves a second-order weak process which is allowed within the Standard Model (SM) as it conserves lepton number.

In recent time, one of the most interesting questions in the field of neutrino physics is whether neutrinos are Dirac or Majorana particles. Neutrino-less double-β decay ($0\nu\beta\beta$) [13] involves a transformation of two neutrons into two protons with the emission of two electrons and no neutrinos. This can only happen if neutrinos and antineutrinos are identical (Majorana particles) and have mass. This process violates conservation of lepton number by two units and is forbidden in the SM of particles. Observation of neutrinoless double-β decay would prove that neutrinos are Majorana particles and would answer the most fundamental question about the nature of the neutrinos. This decay was first suggested by Furry [13] and it is described by the following decay equation:

$$(Z,A) \rightarrow (Z+2,A)+2e^{-} \tag{1.11}$$

The graph of Figure 1.4(a) shows the two-neutrino double-β decay where two electrons and two antineutrinos are ejected from the nucleus. The graph of Figure 1.4(b) shows the neutrino-less double-β decays where two neutrons transform into two protons with the emission of two electrons and no neutrinos.

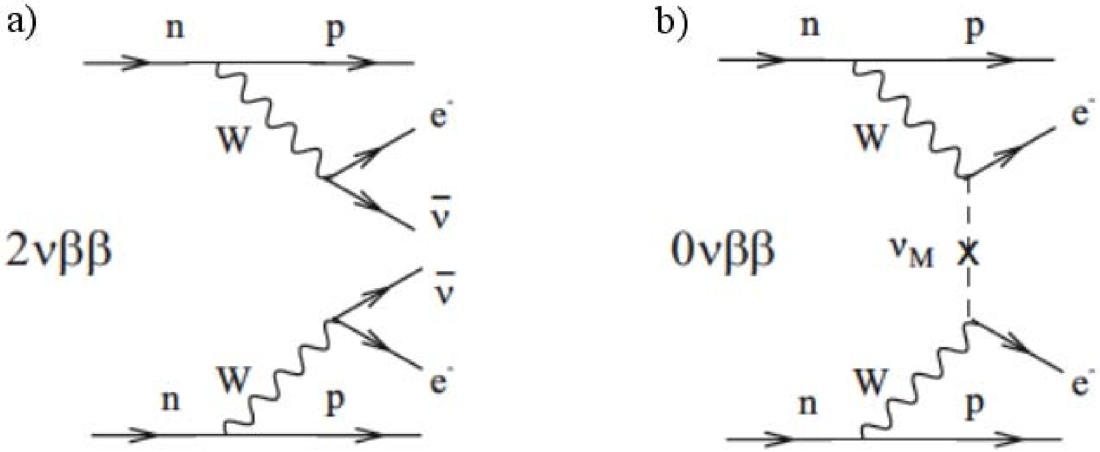

Figure 1.4: Feynman diagram of neutrino ($2\nu\beta\beta$) and neutrinoless ($0\nu\beta\beta$) double-β decay. (Reprinted with permission from Ref. [10].)

1.2.2 Double-β Decay and Nuclear Matrix Elements

As mentioned in section 1.2.1, if $0\nu\beta\beta$ is observed then the neutrino has to be Majorana particle and the effective Majorana mass of neutrino, $\langle m_{\beta\beta}\rangle$ can be deduced from Eq.

$$\left(T_{1/2}^{0\nu}\right)^{-1} = G^{0\nu} \mid M^{0\nu} \mid^{2} {g_A}^{4} \left\langle m_{\beta\beta}\right\rangle^{2} \tag{1.12}$$

where $T_{1/2}^{0\nu}$ is the observed half life of the $0\nu\beta\beta$ decay, $G^{0\nu}$ is the leptonic phase-space factor [14], g_A is the effective axial-vector coupling constant and $M^{0\nu}$ is the $0\nu\beta\beta$ nuclear matrix element (NME), which is entirely based on theoretical calculations. The calculations of $M^{0\nu}$ are performed using several frameworks, such as quasi-particle random phase approximation (QRPA) [15], shell-model [16] and interactive boson model (IBM2) [17]. However, when the $M^{0\nu}$ calculations are compared with each other deviation arises by factors up to 5. In order to extract the $\langle m_{\beta\beta} \rangle$ with precision and accurately from Eq. 1.12, NME needs to be calculated accurately. For double-β decays the theoretical framework used to describe $2\nu\beta\beta$decays can also be applied to $0\nu\beta\beta$ decays. In this situation, the experimental values of NME offer a possibility to benchmark the underlying theoretical calculations. Experimentally, it is possible to determine the $2\nu\beta\beta$ decay NME to benchmark these frameworks by measuring EC and β^- branching ratio of intermediate transition nuclei in double-β decays. Because this measurement directly gives access to the transition through the lowest intermediate state in the $2\nu\beta\beta$ decays, which carries the relevant information for calculating NME. However, the EC transitions are several orders of magnitude weaker compared to dominating β branch and the difficulty of this method arise from this dominating β background. To observe these weak EC branches, these studies require a low-background, high sensitive decay spectrometer.

1.3 Interaction of Photons with Matter

In this section the basic concepts and mechanisms of photon interactions with matter are briefly summarized. According to the framework of SM, photons are massless, uncharged particles and have different characterization based on energy [18]. Because of their electrically neutral behavior, they do not steadily lose energy via Coulombic interactions with atomic electrons as do charged particles and therefore cannot be directly detected. Photons need to undergo interactions with some target materials to detect and measure their energy. In these interactions a photon transfers partial or all of its energy to an atomic electron of the target material [19] and as a result of these interactions, x-rays or γ-rays can be either completely absorbed in the detection materials or scattered with significant energy loss, producing high energy electrons [20]. The most probable and significant photon interactions, photoelectric absorption, Compton scattering and pair production, are described in this thesis.

1.3.1 Photoelectric Absorption

In the photoelectric absorption process a photon interacts with an absorber atom and transfers all of its energy to an electron in that atom [20]. If the incoming photon has sufficient energy, it can liberate a bound electron and produce an energetic photoelectron from one of the shells of the absorber atom. The photoelectric effect requires interaction with the atom as a whole and cannot take place with a free electron since conservation laws for energy and momentum would be violated. The energy that the photoelectron will carry off is given by:

$$E_e^- = h\nu - E_b \tag{1.13}$$

where E_e^- is the kinetic energy of the photoelectron, h is Planck's constant, ν is the frequency of the incoming photon and E_b is the minimum energy required to liberate an electron from an atom, also known as the binding energy [20]. An ionized absorber atom is created with a vacancy in one of its bound shells. This vacancy is subsequently filled by an electron from higher orbital and results in the emission of a photon (characteristic x-ray), which is briefly described in the section 1.1. Either one of two things can happen with this emitted fluorescent photon, it can leave the absorber atom, or it can be reabsorbed and transfer all its energy to an higher shell electron, causing additional ionization and excitation of the atom. Electrons emitted following the interaction with a fluorescent photon are called Auger electrons after Pierre Auger, who first observed this phenomena. The photoelectric process is illustrated in Figure 1.5. The photoelectric effect is the dominant mode of interaction of the x-rays or γ-rays of energy less than 100 keV. The cross-section (σ) for the photoelectric effect decreases with increased photon energy and is enhanced for absorber materials of high atomic number Z. This relationship is roughly approximated by

$$\sigma \sim C \times \frac{Z^n}{E_\gamma^{3.5}} \tag{1.14}$$

where the exponent n varies between 4 and 5 over the x-ray or γ-ray energy region of interest, C is a constant and E_γ is the energy of incoming photon.

1.3.2 Compton Scattering

An elastic collision event between an incident photon and an electron in the absorbing material is termed Compton scattering in honor of the American physicist Arthur Compton [21]. In a Compton scattering event an incident photon of energy $h\nu$ transfers part of its energy to a stationary atomic electron, which recoils with a kinetic energy E_K at an angle ϕ with respect to the direction of the incident photon. After the scattering event, the photon is deflected with an angle θ from its original direction with a lower energy $h\nu'$. Figure 1.6 shows a representation of the Compton scattering event. The transfer of incident photon energy can vary from zero to large value depending on the

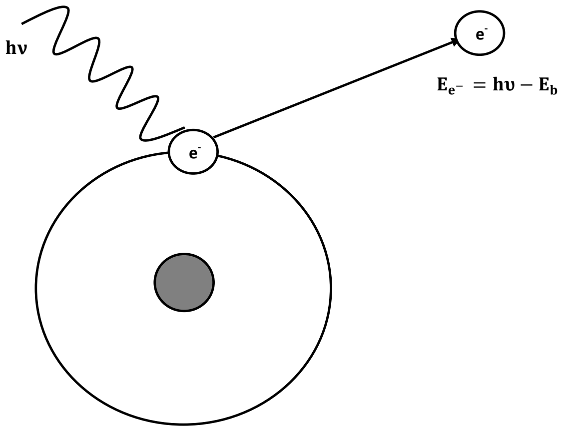

Figure 1.5: Photoelectric absorption showing the incoming photon ejecting the photoelectron. The photoelectron energy is given by Eq. 1.13. When the vacancy left by the photoelectron is filled, energy is released either as an x-ray or Auger electron.

scattering angle. The energy carried off by the scattered photon and the energy of recoiling electron are given by Eq. 1.15 and Eq. 1.16, respectively:

$$h\nu' = \frac{h\nu}{1+\alpha(1-\cos\theta)} \tag{1.15}$$

$$E_e^- = h\nu - h\nu' = h\nu\frac{\alpha(1-\cos\theta)}{1+\alpha(1-\cos\theta)} \tag{1.16}$$

where $\alpha = \frac{h\nu}{m_0 c^2}$, m_0 is the mass of the electron, c is the speed of light and θ is the deflection angle of the scattered photon. Based on the interaction angle between the incoming photon and atomic electron, maximum and minimum energy for the scattered photon can be easily calculated using Eq. 1.15 and 1.16, respectively. If the scattering angle is 0°, the scattered photon has maximum energy, $h\nu' \approx h\nu$ and electron recoil energy, $E_e^- = 0$. For photon scattering angle $\theta \approx \pi$, the incident γ-ray is back-scattered and the electron recoils with maximum recoil energy in the direction of the incident γ-ray. Basically, these equations show that as scattering angle increases, the energy of scattering photon decreases and opposite scenario happens for the recoil electron. The back scattering γ-ray energy and recoil energy are given in Eq. 1.17 and Eq. 1.18, respectively.

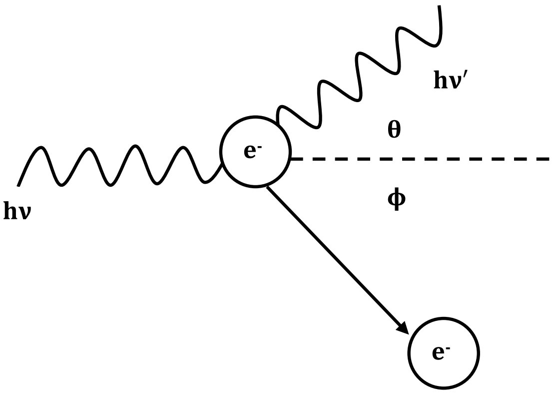

Figure 1.6: Schematic representation of a Compton scattering event between an incident photon of energy $h\nu$ and a stationary atomic electron. After the scattering event photon is deflected by angle θ and electron is recoiled with an angle ϕ with respect to the direction of the incident photon.

$$h\nu' \mid_{\theta=\pi} = \frac{h\nu}{1+2\alpha} \tag{1.17}$$

$$E_e^- \mid_{\theta=\pi} = h\nu \frac{2\alpha}{1+2\alpha} \tag{1.18}$$

The probability that the Compton scattering will happen at a particular angle was studied and established by Oscar Klein and Yoshio Nishina in 1929 [21], and their angular distribution of Compton scattering is described by Eq. 1.19:

$$\frac{d\sigma}{d\Omega} = Z{r_0}^2 \left(\frac{1}{1+\alpha(1-\cos\theta)}\right)^2 \left(\frac{1+\cos^2\theta}{2}\right) \left(1+\frac{\alpha^2(1-\cos\theta)^2}{(1+\cos^2\theta)[1+\alpha(1-\cos\theta)]}\right) \tag{1.19}$$

where r_0 is the classical electron radius. According to this equation, the probability of Compton scattering per absorber atom linearly increases with increasing atomic number Z of the absorber material and gradually decreases with increasing energy of the incident photon [20].

1.3.3 Pair Production

In the pair production process, the incident photon interacts with the Coulomb field of the nucleus. In this interaction process the incident photon disappears and some of the energy of the photon is

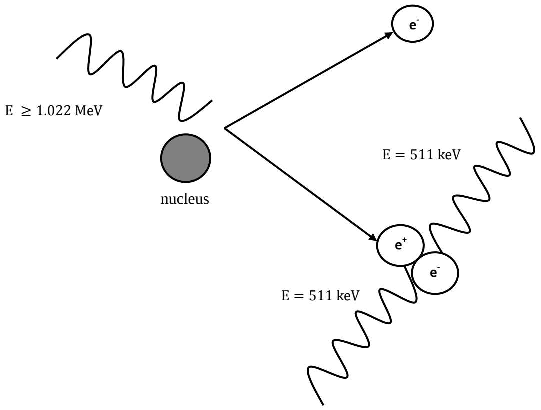

Figure 1.7: Schematic representation of the pair production process showing interaction of an incident γ-ray with the electric field of the nucleus and the subsequent creation of an electron-positron pair.

converted into an electron-positron pair. To conserve energy and momentum this pair production is prohibited in free space [22]. The pair production can only occur if the incident photon has a threshold energy greater than twice the electron rest mass ($2m_ec^2$ = 1.022 MeV) [3]. Pair production is the predominant process for high energy γ- rays. The excess energy is converted into the kinetic energy of the electron and positron pair [20]. The electron and positron travel only a short distance in the absorber medium, transferring their kinetic energy via Coulomb scattering, ionization and excitation. Once the kinetic energy has been reduced to approximately thermal energy, the positron annihilates with an electron in the absorbing medium, creating two back to back 511 keV photons. The pair production process with the creation of annihilation radiation is shown in Figure 1.7. The time required for the positron to reach thermal energy and final annihilation process is estimated to be in the range of ns, and so the annihilation radiations appear in coincidence with the original pair production interaction. There is a probability that each of the annihilation photons can then interact with the surrounding absorbing medium via the photoelectric effect or Compton scattering.

1.4 Semiconductor Detectors

1.4.1 Why Semiconductor Detectors?

Semiconductor detectors are made of crystalline semiconductor materials [23]. These detectors are extensively used in nuclear physics and high energy physics for precision tracking that allows detection of secondary vertexes of very fast decaying particles. Silicon and germanium are the most common materials used for particle detectors; silicon is used in Si(Li) detectors for x-ray detection as in this work, and germanium is used in HPGe detectors for γ detection. Details about these detectors will be discussed in the next chapter. The benefits of semiconductor detectors include:

- The energy band gap between valance and conduction band is small e.g. 1.11 eV for silicon (shown in Figure 1.8) and so the average energy required to create a electron-hole pair is 3.6 eV. This value is a few orders magnitude smaller than the ionization energy required for gases used in proportion chambers [23].
- Because of the high density of semiconductor materials, the average energy loss of an incident particle is relatively high compared to the energy loss in gases. For the case of silicon, the stopping power is 380 keV/mm, whereas for the gases the loss is three orders of magnitude lower [24]. The high density also reduces the range of secondary electrons, which leads to better spatial resolution.
- High mobility of charge carriers (electrons - 1450 cm^2/Vs, holes - 450 cm^2/Vs) allow rapid charge collection ($\approx$10 ns) and short dead times, these properties make semiconductor detectors unique and especially suitable for high event rate experiments.
- Current semiconductor production technology can assemble structures in μm range dimensions that are mechanically rigid and self supporting.

Some disadvantages of semiconductor detectors include high cost and very low operating temperature. One of the possible problems with semiconductor detector crystals is radiation damage. If this happens, then the detectors need to be annealed at high vacuum. An annealing station has been built at the Nuclear Science Laboratory of Simon Fraser University for repairing HPGe detectors crystals. Details of this work will be explained in the experimental setup section.

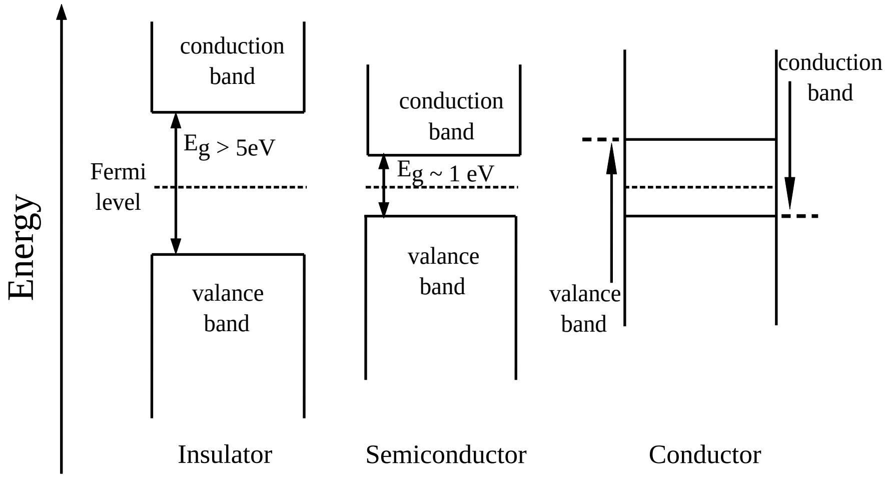

Figure 1.8: Band structure for electron energy in insulator, semiconductor and conductor.

1.4.2 Charge Carriers in Semiconductors

According to the semiconductor band theory, electrons are organized in bands with different energy levels [23]. The lattice structure of crystalline materials creates a periodic potential resulting in two energy bands for solids named the conduction band and valance band, respectively. The lower energy band is called the valance band and its electrons are tightly bound and not free to move. The next higher energy level is called the conduction band, and its electrons have enough energy to become free from the bound state and move freely within the entire crystal structure [20]. Figure 1.8 shows the energy band configurations for insulators, semiconductors and conductors.

Typical semiconductors are group IV elements and have 4 electrons in their valence shell. The energy gap between valence and the conduction bands is called the band gap, and has no energy levels available for electrons to occupy. If a valence band electron is excited by an external energy (e.g. photon, etc.) into the conduction band, then it can participate in the conduction process. Such excitation creates a hole (absence of an electron) that behaves as positively charged particle. Pure semiconductors are called intrinsic semiconductors and contain an equal density of electrons and holes.

It is possible to replace some semiconductor atoms in the crystal structure with atoms from group III or V to increase the charge carrier density, a process known as doping. Group III elements have 3 valence electrons which can easily form covalent bonds with surrounding semiconductor atoms.

This vacancy represents a hole and so group III elements are known as acceptors. Elements from the group V are known as donors and 4 of the 5 valence electrons can make covalent bonds with surrounding semiconductor atoms. The fifth electron is weakly bound and can be easily excited to the conduction band. Heavily doped semiconductors are marked n^+ or p^+, respectively. Because of thermal excitation, both n^+ and p^+ type semiconductors have opposite charge carriers known as minority carriers. According to [23] the intrinsic charge carrier density of a semiconductor at thermal equilibrium is:

$$n(T) = \int_{E_g}^{\infty} D_e(E,T) f_e(E,T) dE \tag{1.20}$$

where $D_e(E)$ is the state density [24]

$$D_e(E) = \frac{1}{2\pi^2} (\frac{2m_e}{\hbar^2})^{3/2} (E - E_g)^{1/2} \tag{1.21}$$

and $f_e(E)$ means the Fermi-Dirac function for a system of fermions

$$f_e(E) = \frac{1}{e^{\frac{E-E_F}{kT}} + 1} \tag{1.22}$$

where E is the energy of electrons, E_F the Fermi level, E_g is the gap energy, T the temperature, k the Boltzmann constant, $\hbar$ the Planck constant, and m_e is the effective electron mass.

1.4.3 Drift and diffusion

Drift and diffusion are the charge transport processes involved in semiconductor detectors. In the presence of an external electric field $\vec{E}$, the movement of electrons and holes are known as drift. The drift velocity $\vec{v}$ is proportional to that electric field

$$\vec{v} = \pm \mu \vec{E} \tag{1.23}$$

where μ is coefficient of the proportionality, representing mobility of electrons. Movement of charge carriers in presence of a magnetic field $\vec{B}$ results in the change of the movement direction by a

Lorentz angle ν_L

$$\tan \nu_L = \mu_H B \tag{1.24}$$

where μ_H is coefficient is known as Hall mobility [25]. Movement of charge carriers as a function of charge carrier distribution is known as diffusion. Electrons and holes move from areas of high concentration to areas of low concentration, creating the diffusion flux $\vec{F}$

$$\vec{F} = -D\vec{\bigtriangledown} n \tag{1.25}$$

where $D = \frac{kT}{q}\mu_H$, q is charge, T is temperature and $\bigtriangledown n$ is charge density gradient.

1.4.4 $p-n$ Junction

In semiconductor detector technology, the most basic concept used is the $p-n$ junction concept. The $p-n$ junction is formed by composing n-type and p-type doped semiconductor together. Because of the gradient of charge density, electrons diffuse from n-type region to the p-type region and leaving behind respective donor atoms which will act as positive charges in their region. Similarly, the opposite scenario happens in the p region with holes, and results in the accumulation of negative space charge in the p region [26]. This diffusion makes two adjacent space charge regions build up the potential barrier between the p^+ and n^+ region which resists further diffusion of charge carriers. This potential barrier is known as the built in potential and this region is known as the depletion region. The magnitude of this barrier depends on the doping level of the n^+ and p^+ regions. Figure 1.9 shows the formation of a depletion region with its electric field and built in potential for the $p-n$ junction. The built in potential of the $p-n$ junction can be represented by Eq. 1.26 [26]

$$V_{bi} = \frac{kT}{q} \ln \frac{N_A N_D}{n_i^2} \tag{1.26}$$

where q is the elementary charge, N_A and N_D are the acceptor and donor doping concentrations in n-type and p-type material, and n_i is the intrinsic carrier concentration in semiconductor.

Radiation passes through the $p-n$ junction of semiconductor detectors and looses energy through interaction with the electrons. Incident particles transfer their energy to electrons through these interactions and promotes electrons to the conduction band to form electron-hole pairs. If ΔE is the

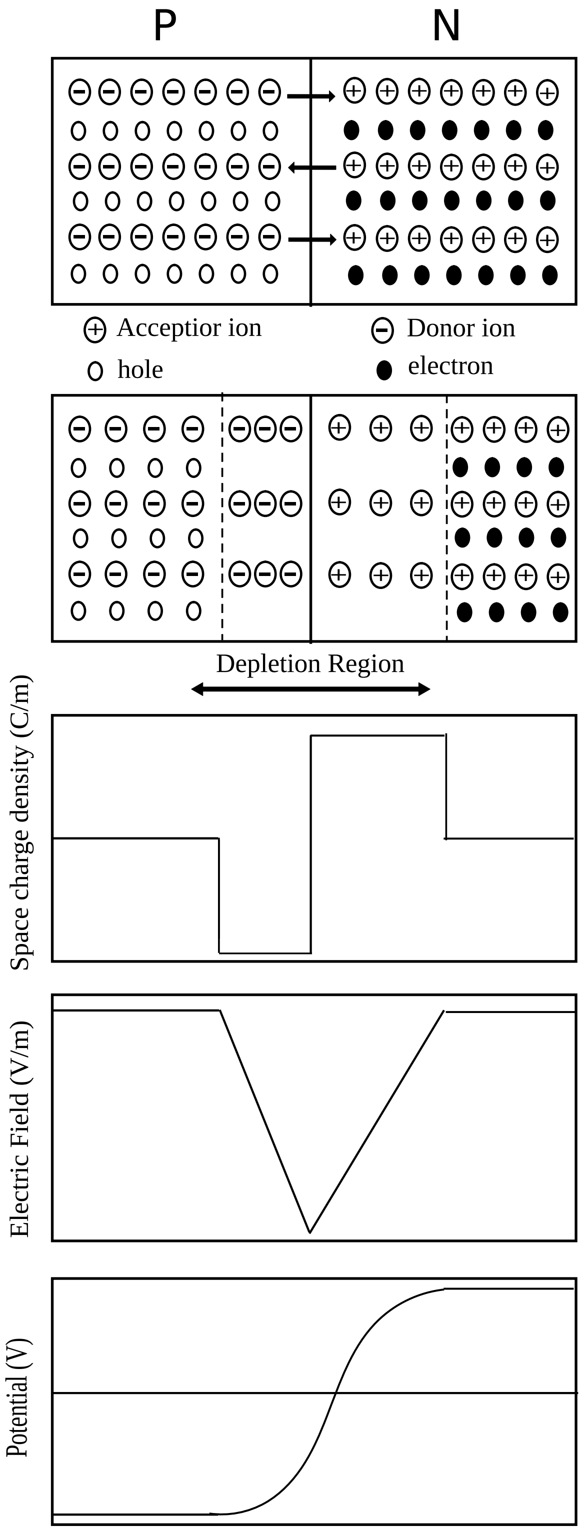

Figure 1.9: The formation of a depletion layer by charge carriers diffusion, space charge density, electric field and built in potential in $p-n$ junction.

total energy loss of incident particles in a $p-n$ junction, then total number of electron-hole pairs produced is:

$$\text{Number of electron-hole pairs } = \frac{\Delta E}{\varepsilon} \tag{1.27}$$

where ε is the average energy required to produce an electron-hole pair. Produced electrons and holes are then swept out by the electric field in the depletion region and accumulated on the n-side and p-side, respectively.

The $p-n$ junction does not provide the best operating characteristics as a particle detectors. The electric field present in the $p-n$ junction is not strong enough to provide efficient charge collection, and the depletion region in the junction is also very thin and not adequate for high energy particles. Improvement can be made to particle detection and the charge collection process by applying a reverse biasing voltage to the $p-n$ junction. Reverse biasing of $p-n$ junction is configured by applying negative potential to the p-side and positive potential to the n-side, respectively. Holes in the p^+ region are attracted from the junction towards the p contact, and electrons in the n-region are attracted from junction to the n contact.

If V_b is the applied potential in reverse biasing a $p-n$ junction, then depletion widths on n^+ and p^+ side, χ_n and χ_n, respectively, can be represent by Eq. 1.28 and Eq. 1.29, respectively according to [26]:

$$\text{Depletion width on n}^+ \text{ region, } \chi_n = \sqrt{\frac{2\varepsilon}{q}\frac{N_A}{N_D(N_A+N_D)}V_b} \tag{1.28}$$

$$\text{Depletion width on p}^+ \text{ region, } \chi_p = \sqrt{\frac{2\varepsilon}{q}\frac{N_D}{N_A(N_A+N_D)}V_b} \tag{1.29}$$

Total depletion width can be represent by Eq. 1.30 [26]

$$W = \chi_n + \chi_p = \sqrt{\frac{2\varepsilon}{q}\frac{N_A+N_D}{N_A N_D}V_b} \tag{1.30}$$

This biasing process will effectively spread the depletion area and therefore increase the sensitivity of the particle detection. Higher external voltage provides a better charge collection, however reverse biasing potential needs to be optimized to protect semiconductor detector from reverse breakdown.

Chapter 2

Experimental Setup

2.1 Radioactive beam production at TRIUMF

TRIUMF, Canada's National Laboratory for Nuclear and Particle Physics is located on the University of British Columbia campus, in Vancouver, Canada. It has one of the world's most advanced radioactive ion beam (RIB) facilities, named ISAC- the Isotope Accelerator and Separator [27]. The ISAC facility with its different experimental halls is illustrated in Figure 2.1. To produce radioactive ion beams, ISAC uses the isotope separation on-line (ISOL) technique, where the short lived nuclei are produced during the interactions of the proton beam with thick targets, and converted to a radioactive ion beam in an ion source.

TRIUMF has the world's largest cyclotron which can accelerate H^- to a kinetic energy up to 500 MeV. A graphite foil is placed in the beam path, which removes two electrons from H^- and leaves only the proton. TRIUMF's cyclotron can deliver up to 100 μA protons at up to 500 MeV to a thick target at the ISAC facility and produce wide range of exotic nuclides through spallation, frangmentation and fission reactions. Through these processes, isotopes can be produced with proton (Z) and neutron (N) numbers less than or equal to the target material. The desired element can then be selectively ionized using ion an source. The ISAC facility has three ion sources for this purpose: a surface ion source, a laser ion source (LIS) and a forced electron beam induced arc discharge source (FEBIAD) [27]. Each specific ion source is used to ionize specific elements or molecules depending on their specific atomic binding energies. A wide range of isotopes are extracted from the ion source using a variable potential from 12 keV to 60 keV. After that, the ionized mixed isotopes are sent to a high resolution mass separator which contains two dipole magnets. In the mass separator specific

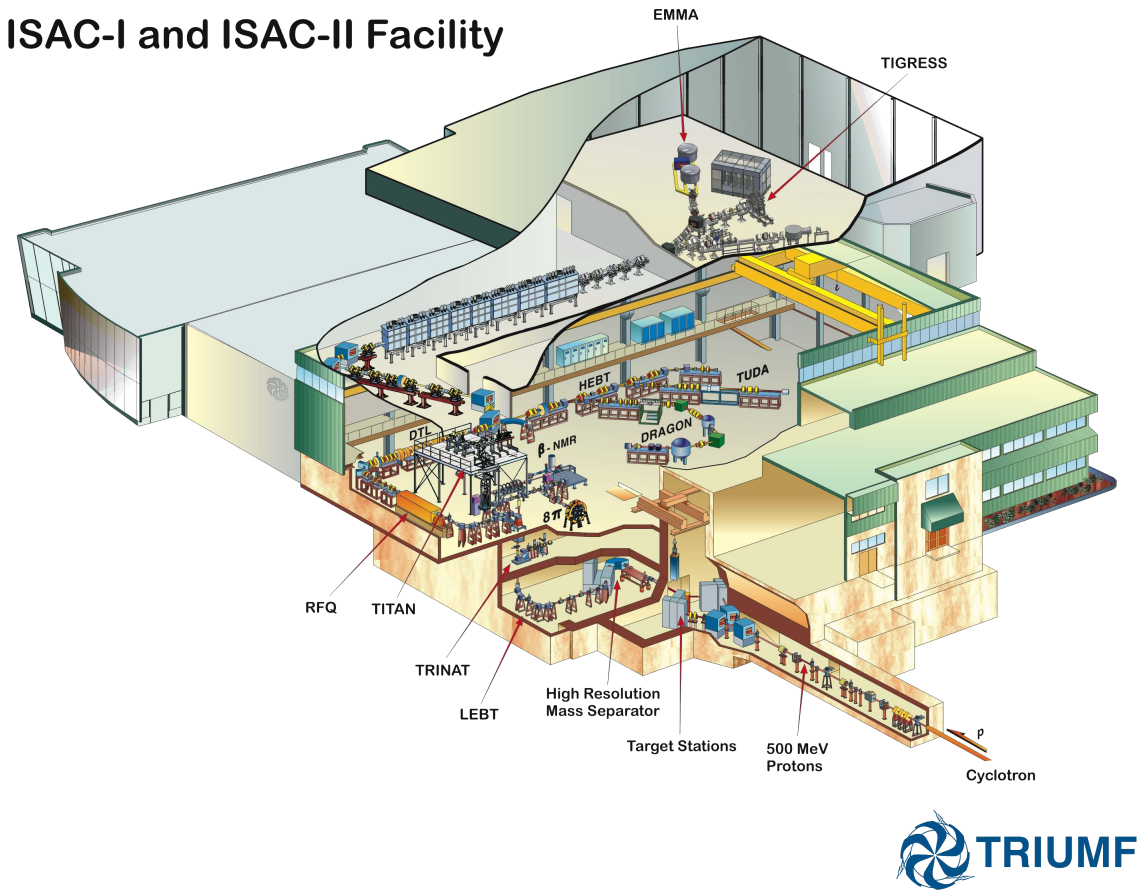

Figure 2.1: A schematics of ISAC-I experimental hall at TRIUMF highlighting different experimental areas. (Adapted from Ref. [28].)

nuclei are selected based on mass to charge ($\frac{m}{q}$) ratio according to Eq. 2.1:

$$r = \frac{1}{B}\sqrt{\frac{2m\Delta V}{q}} \tag{2.1}$$

where r is the radius of a circular orbit, m is the mass of the ionized isotope, B is the applied magnetic field, q is charge of the isotope and ΔV is the potential difference between the ion source and mass separator. This mass separator can distinguish between isotopes with resolution, $\frac{\Delta m}{m} \approx \frac{1}{2000}$. The produced RIBs are finally guided electrostatically to different experimental areas located in the ISAC facility one of which is TITAN [1].

2.2 TITAN overview

The TRIUMF Ion Traps for Atomic and Nuclear Science (TITAN) [29, 30] facility is located in the low energy area of the ISAC facility (see Figure 2.1). TITAN's main goal is to perform high precision experiments of short lived radioisotopes using ion traps. For this purpose TITAN uses three main components; a gas-filled linear Radio-Frequency Quadrupole cooling ion trap (RFQ) [31, 32] for cooling and bunching the radioactive beam; an Electron Beam Ion Trap (EBIT) for charge breeding to create highly charged ions (HCIs) and for performing in-trap x-ray and γ-ray spectroscopy; a Penning ion trap (MPET) [33] for high precision mass measurements. In the near future, two more components will be added to TITAN facility; a cooler Penning ion trap (CPET) to cool the HCIs before mass measurement [34], and a multi-reflection time-of-flight (MR-TOF) apparatus [35] for beam purification. In addition, there is an off line source, which can be used for equipment testing and optimization. A schematic layout of TITAN's main components is shown in Figure 2.2.

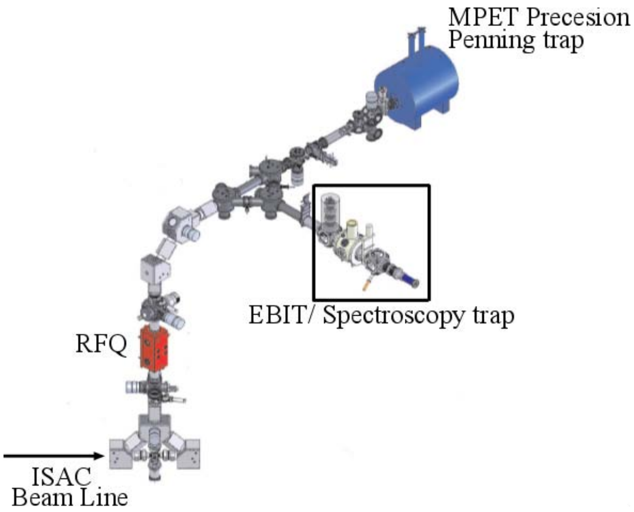

Figure 2.2: A schematic view of the TITAN facility at TRIUMF. During the time of decay spectroscopy experiments radioactive ions are injected in to the RFQ from the ISAC beam line. Ions are bunched and cooled in the RFQ and then injected into the EBIT where they are stored for decay spectroscopy. (Reprinted with permission from Ref. [31])

For experiments, radioactive ion beams are guided and delivered by the ISAC accelerator to TITAN. Incoming ions have a kinetic energy up to 20 keV with a few eV energy spread ($\frac{\delta E}{E} \approx 10^{-4}$) [36]. For precision mass measurements, TITAN MPET needs beams with kinetic energies in the range of a few eV with very small energy spread. In the RFQ, beams are cooled via collisions with a neutral buffer gas normally helium and then converted to a bunch form at a given energy by the RF quadrupole and a longitudinal electric field. Afterwards, the bunched ions can be sent to MPET for precision mass measurements or towards EBIT for charge breeding. Charge breeding prior to mass measurement will increase the precision of the measurements [37]. In the case of ECBR measurements, RIBs are sent directly to the EBIT from the RFQ, where bunched ions can be trapped with or without charge breeding to perform decay spectroscopy using a Si(Li) detector array.

This thesis only focuses on modeling and simulation of the ECBR measurement apparatus EBIT and its detector array.

2.3 Electron Beam Ion Trap (EBIT)

The TITAN EBIT [38] was designed and built in 2005 in collaboration with the Max-Planck-Institute for Nuclear Physics (MPIK), Heidelberg, and commissioned on-line at TRIUMF in November 2008 [33, 39]. The EBIT trap structure consists of a series of cylindrical electrodes, similar to a Penning trap although operating on a slightly different principle. The main components of an EBIT are the high intensity electron gun, the magnet chamber, the drift tube assembly and electron collector. Figure 2.3 shows a cross section of the trapping region of the TITAN EBIT.

The TITAN EBIT is designed to provide an electron beam with maximum energy of 70 keV and intensity up to 500 mA (an upgrade to 5 A is foreseen). The EBIT features a trap structure with nine conical shaped electro-polished, oxygen-free, high-purity copper drift tubes as shown in Figure 2.3, which is optimized for operation with an electron beam [41]. The drift tubes are thermally connected to a superconducting magnet at $\approx$ 4 K. The central drift tube is eight-fold segmented, and has an inner radius of 7 mm. The guard electrode is sixteen-fold segmented, with an inner radius at the outermost position of 7.5 mm gradually reducing to 2.5 mm. These segmented central electrodes provide visible access to the trap center. Ions are trapped inside the central drift tube for charge breeding or decay spectroscopy.

The TITAN EBIT can produce up to 6 T magnetic field by two Nb_3Sn superconducting coils in a quasi-Helmholtz configuration. The superconducting coils are 55 mm wide with inner and outer a diameters of 115 mm and 216 mm, respectively. The two coils are separated from each other at a distance around 112 mm. The distance is larger than the coil radius, and this results in a magnetic field minimum at the EBIT center. At the trap center, magnetic field is reduced by 8%, which creates

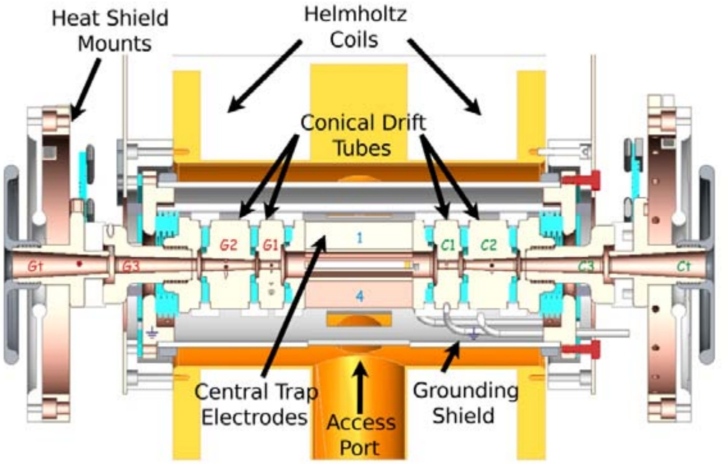

Figure 2.3: Cross section of the trapping region of the TITAN EBIT. The trap drift tubes are labeled out from the central drift tube towards either the electron gun (G) or collector (C). The ion bunch is injected and extracted from the collector side of the trap by applying potential to the four segments of the conical drift tubes. Ions are trapped in central drift tube forming a prolate spheroidal shape, within a 70 mm of axial volume. (Reprinted from Ref. [40])

a magnetic bottle effect [10]. As mentioned earlier, there are access ports on the EBIT for detector attachments to perform decay spectroscopy. These access ports are covered by two thin (250 μm outer window and 80 μm inner window) Be windows, which provide vacuum separation and thermal shield to the trap. In this configuration, the access ports provide visible line of sight to the center of trap. Considering all these dimensions and materials, a detailed model of the EBIT was created; as seen in Figure 2.4.

The EBIT can be used to trap ions and to perform x-ray and γ-ray spectroscopy while charge breeding. Applying electrostatic potential to the EBIT electrodes confines the trapped ions axially, while the space charge of the electron beam and magnetic field confines them radially, as seen in Figure 2.5. Charge breeding electrons are emitted in a low magnetic field and attracted by the trap potential. As they move towards the trap center, they are compressed by the strong magnetic field. This compression can raise the electron beam current density up to 105 A/cm^2 [10].

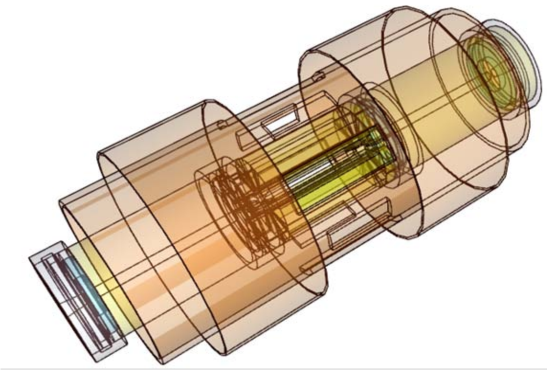

Figure 2.4: GEANT4 simulated 3D model of EBIT. The centre structure is made of series of cylindrical electrodes made of pure Cu. Electrodes are separated by insulating materials such as Al_2O_3 and macor. Electrodes are segmented and have slit structure to access center of the trap for decay spectroscopy.

2.4 TITAN-EC

Measurements of ECBRs are generally carried out using conventional tape station techniques, where a radioactive sample is implanted in a carrier material (usually mylar tape) and then moved in front of several detectors to observe x-rays and β particles. Once this measurement is complete, a new sample is implanted, and the measurement cycle is repeated. The schematic of a conventional tape station for ECBR measurements is shown in Figure 2.6. This process suffers from x-ray attenuation in the carrier material where radioactive isotopes are implanted. Isobaric contamination is an important issue as well. The most important limiting factor of this conventional technique is the intense β background from dominating β branches. By vetoing beta particles, this background can be reduced, but not suppressed completely [1].

To overcome these drawbacks, TITAN-EC has developed a novel technique where ions will be stored in a backing free environment in the center of the EBIT trap. Here, the x-rays following EC from the daughter nuclei of the trapped ions will be observed using a high resolution semiconductor (Si(Li)) detectors. The trap's strong magnetic field will guide all electrons originating from β decays away from the detectors, and allow ECBR measurements to be performed in a reduced background environment [1].

In the ECBR measurement, purified, cooled and bunched radioactive ions will be sent from the TITAN RFQ to the EBIT. The charged ions will be confined axially by applying an electrostatic

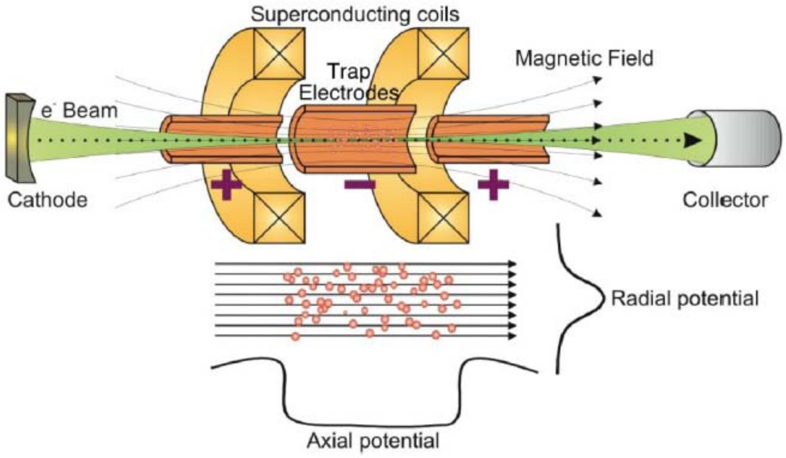

Figure 2.5: Basic working principle of electron beam ion trap (EBIT). This diagram is showing EBIT's electron gun assembly, magnetic coils and drift tube assembly with a typical trapping potential. (Reprinted with permission from Ref. [42]).

potential to the drift tube electrodes and radially by a 6 T magnetic field. When ions are trapped and stored, charge breeding is also possible. A schematic diagram of trapped ions in the EBIT is displayed in Figure 2.7.

The versatile EBIT geometry allows x-ray detectors to be mounted close to center of the trap. Seven external ports allow the mounting of 50 mm radius, planar Si(Li) detectors for performing spectroscopy on trapped ions. In order to minimize the absorption of x-rays on their way to the detector, these access ports are covered with 250 μm thin Be window to provide vacuum isolation to the EBIT. Another 80 μm thin Be window, which act as a heat shield for the cryogenic system of the superconducting magnet, is located 225 mm from the trap center at the opening of access port [31].

Corresponding to the large slits in the electrode housing, three 8-inch access ports are located at angles 90°, 180° and 270° relative to the cryo-cooler, which is located at the top 0° position. Four 6-inch access ports are located at the diagonal positions at the angles 45°, 135°, 225° and 315°. A cross section of the geometry for the EBIT coil holder, central drift tube electrode and position of the access ports, as implemented in GEANT4 is presented in Figure 2.8 and CAD model is presented in Figure 2.9, respectively. This configuration of the EBIT, with seven mounted Si(Li) detectors,

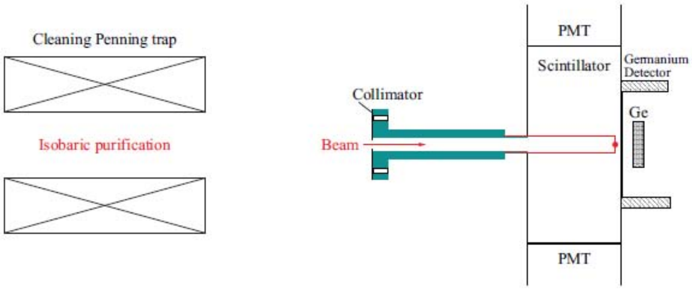

Figure 2.6: The schematic view of a conventional tape station for ECBR measurements. This experimental setup is used to the measure ECBR of ^{100}Tc. (Reprinted with permission from Ref. [36].)

provides total solid angle coverage of $\approx 2.1\%$.

2.5 Si(Li) Detectors

The lithium drifted silicon detectors (Si(Li)) for TITAN-EC are designed and constructed by Canberra. Each planar Si(Li) detector contains a 5 mm thick crystal with a 0.1 μm dead layer. Each detector has 2000 mm^2 total active surface area, and the crystal is located 7 mm from the front carbon window (see Appendix A for more details dimensions of the Si(Li) detector). This carbon layer is 0.6 mm thick and acts as a vacuum and thermal shield for the crystal.

Si(Li) crystals are kept and operated at liquid nitrogen (LN$_2$) temperature to reduce thermally generated leakage current and Johnson noise. The ISAC-EPICS [25] system controls the LN$_2$ supply from the cryostat to each individual detector dewar. To reduce ambient background signals in the crystals, the outer casing of each detector crystal is covered by a low activity 1 mm thick lead shield, surrounded by a 2 mm thick copper shield. These shields prevent radiation from entering from the side of each detector, and reduce the overall ambient background contribution to the measured spectra by a factor of 3-4 [24].

For signal processing, the detectors contain Canberra PSC 854 transistor-reset pre-amplifier with a positive energy and timing signal output. The pre-amplifier's built in alarm card provides notification in the event of detector warm up. A 28 V DC power supply is used for detector's pre-amplifier. A passively cooled linear voltage regulator with output of DC ±12 V and ± 24 V is used

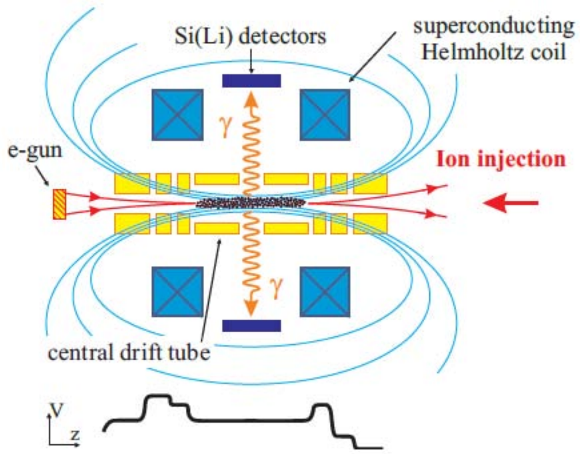

Figure 2.7: A schematic view of TITAN-EC operation for decay spectroscopy. Trap electrodes, Si(Li) detectors, Helmholtz coils and the ions injection or extraction site are displayed in this diagram. Also, the detection geometry for x/γ-rays using the Si(Li) detectors, the magnetic field that will guide β electrons out of the trap and the trap potential on the axis are indicated. (Reprinted with permission from Ref. [31].)

separately for individual detector electronics. This voltage regulator can provide output within the ±1 mV range. An ISEG EHS 8210x high-precision high voltage (HV) power supply with 8 channels is used to bias the detector crystals between -500 V to -700 V. The CAN-interface is used to control the detector's power supply and shuts down the HV supply automatically in the event of detector warm up [40].

Planar Si(Li) detectors have good resolution and high efficiency at photon energies below 50 keV [43]. These detectors were chosen for high-sensitivity x-ray measurements over high-purity germanium (HPGe) crystals due to their decreased x-ray escape peak intensity [1]. As mentioned earlier, there are seven access ports around the EBIT which houses seven Si(Li) detectors for the in trap spectroscopy experiment. The aluminum frame structure was built at the SFU machine shop to support all detectors around the central plane of EBIT, which is mounted at the base of the magnet housing. Figure 2.10(a) shows Si(Li) detectors 1, 2, and 3 are surrounding the southern hemisphere of EBIT, and figure 2.10(b) shows the front face of the Si(Li) detector with carbon window and passive shielding.

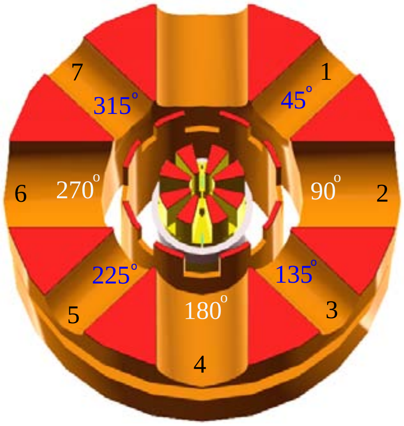

Figure 2.8: A cross-section of the GEANT4 geometry for the magnet coil holder, eight-fold segmented central electrode, and housing cylinder, showing the locations for optical access to the trap center. The port angles are given in degrees for the large (blue) and small ports (white). All angles are shown relative to 0°, where the EBIT cryo-cooler is located. When facing the electron gun, the numbering convention for the seven open ports starts with 1 at 45° and moves clockwise around the trap.

2.6 Electronics

A custom amplifier was developed at SFU for amplifying and filtering signal in TITAN-EC. Signals from the detector's pre-amplifier is connected to this signal processing amplifier before digitizing with an analog to digital converter (ADC). The step by step operating principle of the amplifier module is illustrated in Figure 2.11. At the first stage, the signal goes through a high pass filter which allows the high frequency, positive step signal to pass through while removing all low frequency background noises. Following the amplification stage, the signal is integrated by attenuating all high frequency noises in a low pass filter. A detailed schematic circuit diagram of the custom amplifier is illustrated in Appendix B.

An 8-channel self-triggered field-programmable gate array (FPGA) based sampling ADC (Struck SIS3302), clocked at 100 MHz frequency is used for signal digitization after processing in amplifier module. This module allows the user to program the signal pulse shaping rise time and trigger threshold level for each channel individually [23]. A programmable pulse generator (PPG) signal from the EBIT is coupled with the ADC. Each triggered event is recorded with a 48-bit time-stamp generated by the ADC clock. Every recorded event contains timing information relative to the start

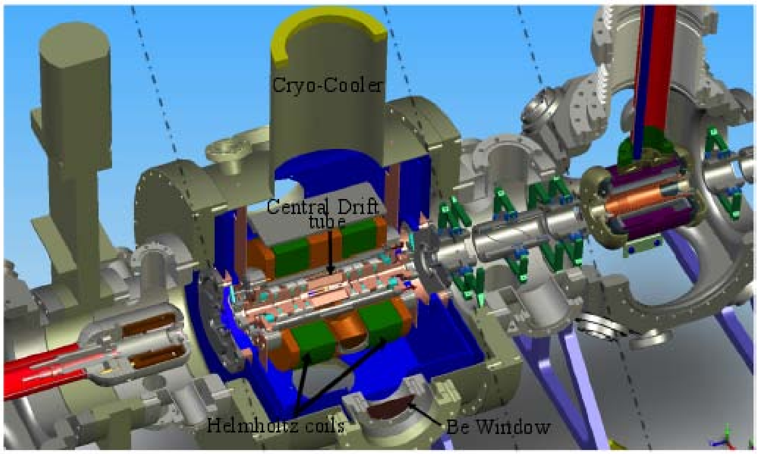

Figure 2.9: A schematic of TITAN EBIT. The access ports are around the central trap for low energy photon detectors and are separated from the trap volume by thin Be windows. (Reprinted from Ref. [40].)

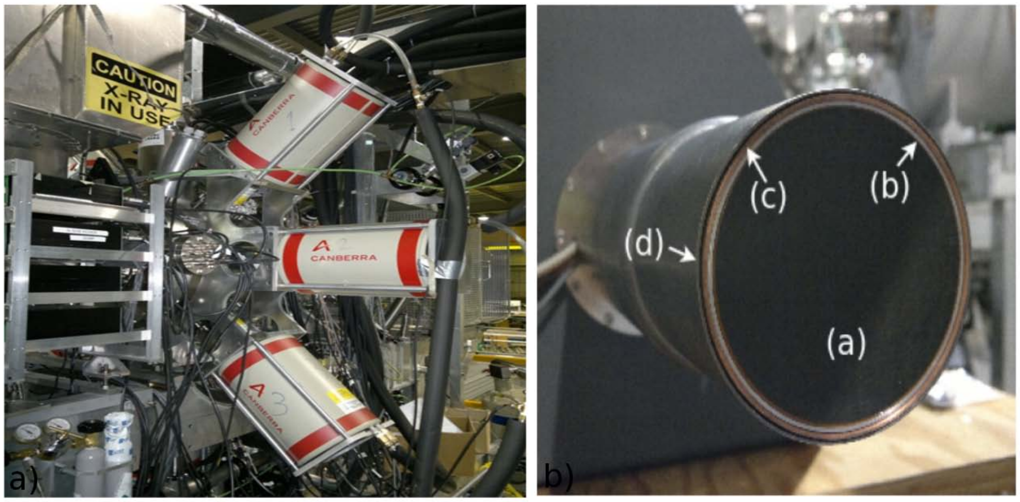

Figure 2.10: a) A photograph of Si(Li) detectors 1, 2, and 3 that surround the southern hemisphere of the EBIT. b) A front view of planar Si(Li) detector showing the thin carbon window (a), the detector's aluminum housing (b), the Cu absorber (c) and the Pb background shields (d). (Reprinted from Ref. [40].)

Figure 2.11: Block diagram of custom built amplifier module showing operating principle.

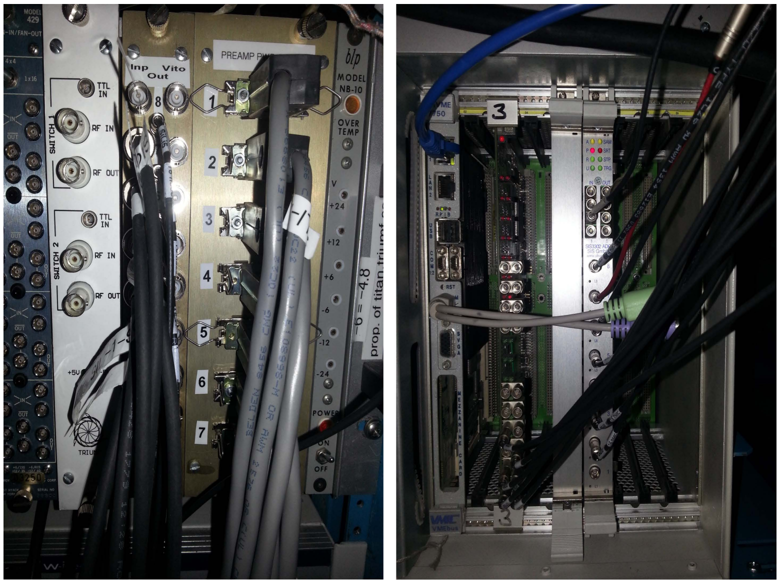

Figure 2.12: A photograph of TITAN-EC electronics modules showing the connections from detectors pre-amplifier to custom built signal processing amplifier and then to self triggered 8-channel SIS3302 FPGA-based sampling ADC for signal digitization.

of each measurement cycle [24]. Figure 2.12 shows the TITAN-EC electronics module's connections from detector's pre-amplifier to custom built signal processing amplifier and then to the self triggered 8-channel SIS3302 FPGA-based sampling ADC for signal digitization.

Chapter 3

GEANT4 Simulations

3.1 GEANT4

The GEometry ANd Tracking (GEANT4) [44] is an open-source object-oriented simulation toolkit developed by an international collaboration of research laboratories and national institutes. The package is developed in the C++ programming language which allows users to simulate the interactions of different particles including electromagnetic, hadronic and optical processes with matter using Monte Carlo methods. This toolkit allows users to construct 3D simulations by defining complex geometries and volumes for detectors and environments. GEANT4 enables the tracking and visualizing of particles for different processes and interactions over a wide energy range, from eV up to TeV energies inside a 3D environment.

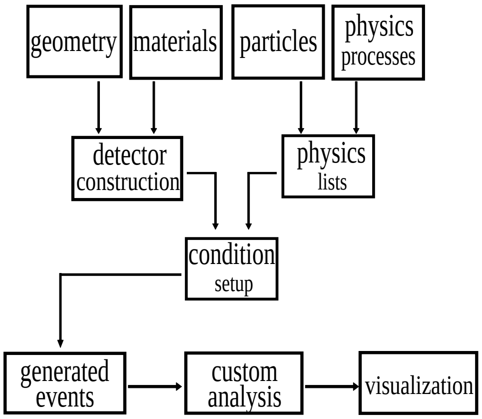

Figure 3.1: Simulation process flow diagram of GEANT4

A set of physical models describing interaction of particles with materials need to be included by the users to specify the physical processes in the simulation. A basic process flow for a GEANT4 simulation is illustrated in Figure 3.1. Originally, the GEANT code was developed for high-energy particle physics simulations. However, in recent time it has been adopted as the leading computation method for nuclear physics, space science and medical physics.

3.2 GEANT4 Simulation of TITAN-EC

3.2.1 TITAN-EC Geometry

The TITAN-EC geometry has been modeled using the GEANT4 simulation package. The geometry of EBIT with superconducting coils was constructed according to the technical drawing of TITAN experimental setup and the geometry of Si(Li) detectors was constructed according to information provided by manufacturer (Canberra). A detailed GEANT4 rendering of the EBIT geometry and Si(Li) detector are presented in Figure 2.4 and Figure 3.2, respectively. Figure 3.2 shows the Si(Li) crystal with a 100 nm dead layer, structure housings, cold-finger, cryostat, and the 0.6 mm carbon window at the front side of crystal.

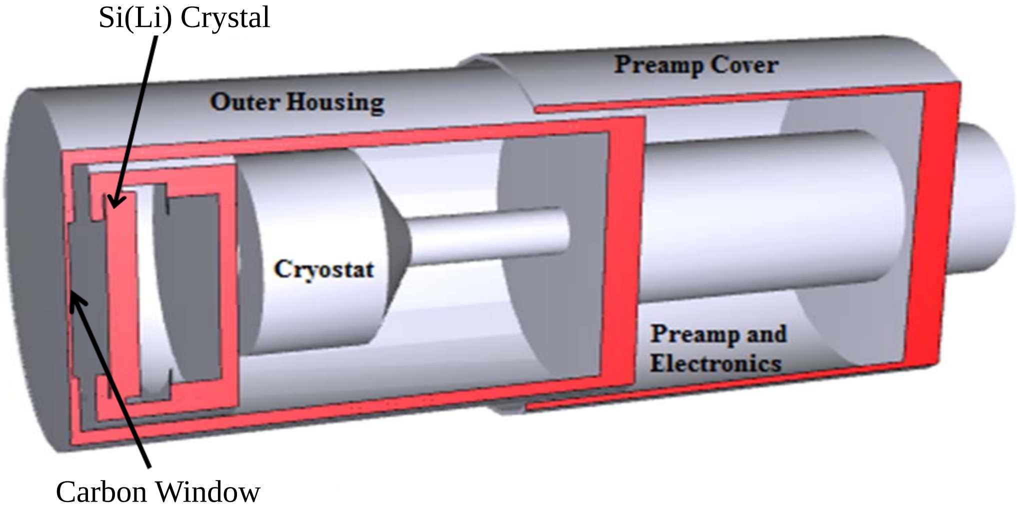

Figure 3.2: A cross-sectional view of the GEANT4 geometry for one of the seven Si(Li) detectors. The geometry includes the Si(Li) crystal with 100 nm dead layer, structure housings, cold-finger, cryostat, and 0.6 mm thick carbon window at the front side of crystal.

Simple shapes, such as cubes, cylinders, cones and spheres or combination of these simple shapes, were used to build up TITAN-EC's complex geometry. A complete GEANT4 geometry of the TITAN-EC experimental apparatus is presented in Figure 3.3.

The geometry build up started by defining a large cube shaped mother volume named ”World” made of vacuum. All components of the TITAN EBIT are placed and added in the World volume relative to its three dimensional reference system. For the entire TITAN-EC geometry construction, the center of the EBIT trap was considered as the reference point in a three dimensional system due to the symmetric geometry. The center of the trap was also reserved for particle emission reference. For the Si(Li) detector geometry construction, another cube shaped volume named ”SiLi” was defined and all parts of the detectors were added on that volume. After constructing the detector geometry, this SiLi volume was added in the World volume to complete total geometry. For proper placement of the detectors, the SiLi volume was rotated by 45° relative to the reference point of the cryo-pump which is located at the top of EBIT, and then placed around the EBIT trap. A cross section of the TITAN-EC simulated apparatus is illustrated in Figure 3.4. Detectors are placed in a way that the carbon window of each detector is 225 mm away from the center of the EBIT trap.

3.2.2 Materials and Physical Processes

In GEANT4, user defined atomic elements are used for all materials. Materials used to built TITAN-EC geometry are defined based on their atomic number and density. All numbers used to define materials in this simulation are taken from Ref. [20, 45]. These defined elements are used to create all materials and alloys with proper density, chemical formula and mixing ratios according to Ref. [46, 47]. In addition to standard materials, macor is also added to the simulation materials class, named Macor. Macor has a density of 2.52 g/cm^3 and is composed of 46% silicon dioxide (SiO_2), 17% magnesium oxide (MgO), 16% aluminium oxide (Al_2O_3), 10% potassium oxide (K_2O), 7% boron trioxide (B_2O_3), and 4% fluorine (F).

The physical processes involved in this simulation are electromagnetic in nature. All the possible processes for the photon, electrons and positrons are defined in TITAN-EC simulation. GEANT's built in physics models are used to calculate the interaction probability for these physical processes [44]. For x-ray and γ-ray, photoelectric absorption, Compton scattering and pair production are included as possible processes. After experimenting with different Compton models, the Penelope Compton model [46] was selected for this simulation to execute Compton scattering processes. For

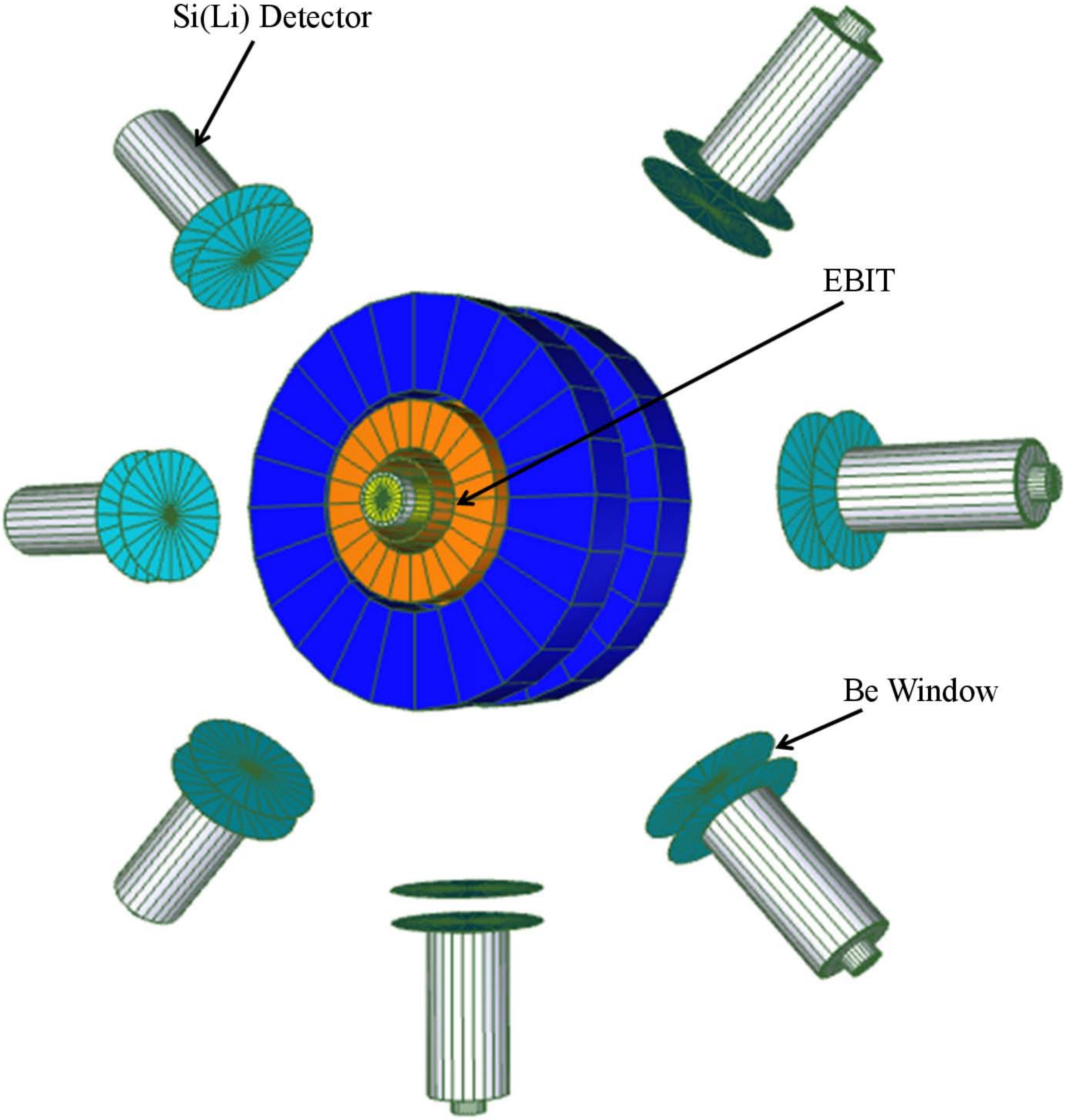

Figure 3.3: Visualization of the GEANT4 simulated geometry of TITAN-EC experimental set-up. The center structure (EBIT trap) is made by a series of cylindrical electrodes including insulating material and Helmholtz coils. Seven Si(Li) crystals are placed radially in front of thin (250 μm and 80 μm) Be windows around the trap.

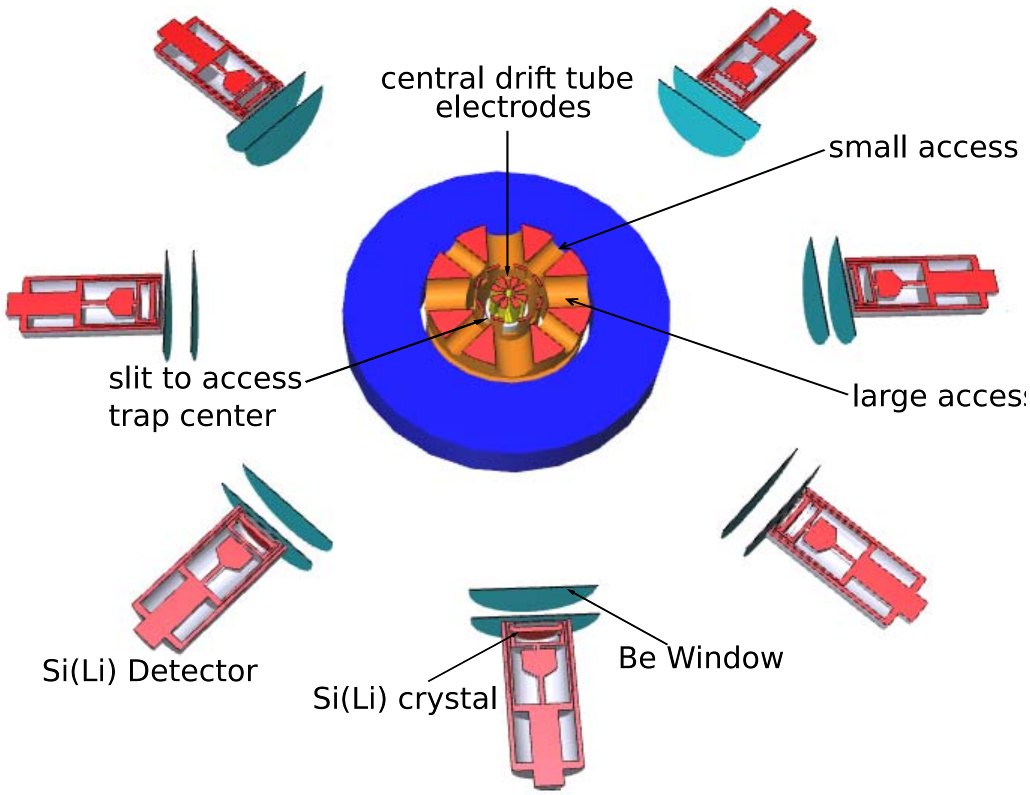

Figure 3.4: Cross section of the TITAN-EC apparatus observed by GEANT4 simulation. Seven Si(Li) detectors are placed 225 mm away from the center of the EBIT trap on the opening of the access ports and separated by thin Be window. The slits in the EBIT housing and superconducting coil configuration provide direct line of sight from Si(Li) detector to trap center.

electrons and positrons, multiple scattering, ionization, bremsstrahlung generation and annihilation processes from built in GEANT4 model lists were included in the physical processes.

3.2.3 Particle Emission

GEANT4's particle gun class handled the particle emission processes in this simulation. Particles (photon, electron, positron) to be emitted are passed to particle gun class with its energy, emission probability, momentum direction and position of origin relative to the center of the trap [48]. Besides, without using the particle gun source user can also choose the General Particle Source (GPS). The angular momentum direction of particles are randomized using random numbers. Uniform random numbers are used between 0 and 1. The random number generator is seeded on system clock to ensure initial randomness during each use. A three dimensional vector (u_x, u_y, u_z) represents the particles angular direction in GEANT4. To generate an isotropic distribution of emitting particles in a 4π solid angle, the following equations are used:

$$\theta = \cos^{-1}(-1+2R_1) \tag{3.1}$$

$$\phi = 2\pi R_2 \tag{3.2}$$

$$(u_x, u_y, u_z) = (\sin\theta \times \cos\phi, \sin\theta \times \sin\phi, \cos\theta) \tag{3.3}$$

where R_i (i = 1, 2) are uniform random numbers. For the TITAN-EC simulation, the particle gun is initialized by ion file parameters, which contains information about the particular isotope's mass number, spin state and radiation decay scheme of that isotope according to known transitions collected from National Nuclear Data Center (NNDC) [49]. A sample ion input file for GEANT4 is presented in the Appendix C.

3.2.4 Simulation Data management and ROOT Implementation

In the initial development stage, information generated by the simulation program was recorded in ASCII format. Each recorded event in the data file contained the event number, particle type and total energy deposited in the each volume of TITAN-EC geometry. In addition, the physics process responsible for this energy deposition is also recorded. Additionally, the three-dimensional position relative to the trap center were recorded for each particle. This information was sufficient to describe the deposited energy in Si(Li) crystals, which can then be used to generate histograms and spectra. Recorded ASCII files were sorted using custom made C^{++} programs to generate histograms. The energy resolution of the Si(Li) detector was modeled during the sorting process, and the energy output from the GEANT4 is recorded within 100 eV bins. However, the simulation output is standardized by keeping simulation and experimental data on the same platform. For standardization, the C^{++} based ROOT data analysis software package is interfaced with the GEANT4 code. ROOT [50] is an object oriented data analysis framework developed by European Organization for Nuclear Research (CERN). When storing simulation data into ROOT, a new ROOT Tree Branch is created for smeared total deposited energy in the Si(Li) crystal according to the detector energy resolution. Python scripts were used for visualizing multidimensional histogram on TITAN-EC's ROOT data structures for analysis purposes. At present stage, users are able to choose simulation output data format by defining data type in macro file (see Appendix C for a sample macro file) at the beginning of every simulation [46].

3.2.5 Efficiencies of Si(Li) Detector

Simulations provide a great opportunity to predict the particle detection efficiency at any given energy range, while calibrated radioactive sources cover only part of energy spectrum. The first characteristic studies performed using GEANT4 simulation was the absolute photon photopeak detection efficiency calculation for a Si(Li) detector. To simulate photon photopeak detection efficiency, 10^6 monoenergetic γ-rays for each energy were fired from a point source particle gun towards the center of the Si(Li) crystal. This simulation was performed in the energy range from 1 keV to 1000 keV with 1 keV steps. To reduce statistical uncertainties, the number of decay events for individual γ-rays energy increased to 25 million for high energies. The γ-ray photopeak detection efficiency for a particular energy can be calculated by the number of the detected γ-rays in the full energy peak dividing by the total number of emitted γ-rays as given by the Eq. 3.4:

$$\varepsilon(E_\gamma) = \frac{N_{E_\gamma}}{A\Delta t I_\gamma} \tag{3.4}$$

where N_{E_γ} is the number of counts for a transition with an energy (E_γ) in the measured spectrum, A is the source activity, Δt is the measurement time and I_γ is the intensity of the γ-ray. For simulation, $A\Delta t$ can be replaced with the total number of decay events used from the particle gun. The simulated γ-ray detection efficiencies of Si(Li) detector are presented in Figure 3.5. The simulation provides the highest efficiency of about 93.71% at 20 keV and 3.71% at 100 keV, respectively.

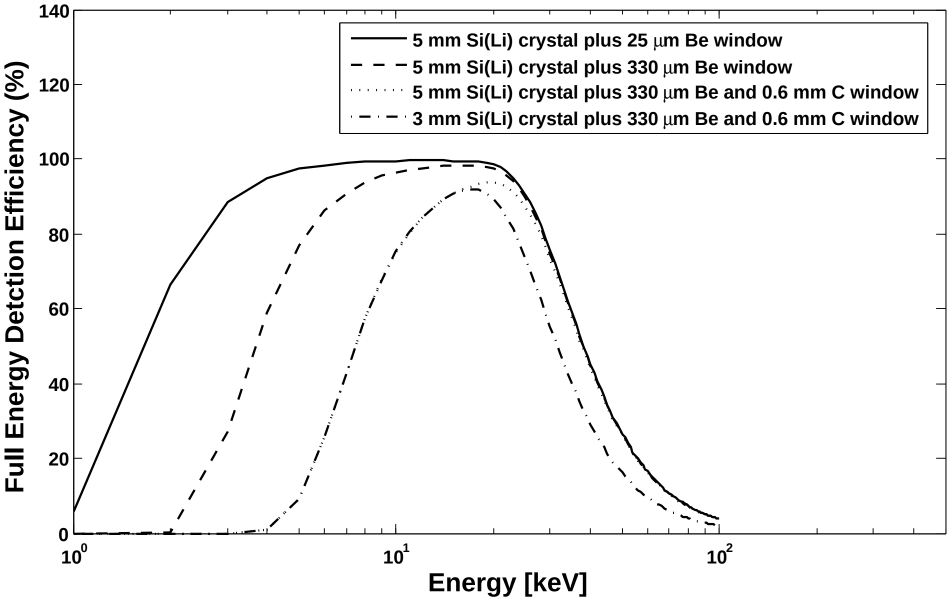

Figure 3.5: The GEANT4 simulated efficiency response of the Si(Li) crystal as function of energy. The observed response of the Si(Li) crystal from source measurement was accomplished by varying the thickness of the C window, Be window and Si(Li) crystal in GEANT geometry.

The Si(Li) detector efficiency is extremely important as it is directly related to the sensitivity of ECBR measurement. The precision of the ECBR measurement is limited by the number of the photopeak counts detected. For accurate measurement of the photopeak detection efficiency, the C window thickness, Be window thickness, Si(Li) crystal and dead layer thickness were varied to match the observed response from source measurements. At low energies, the Si(Li) detector's efficiency is limited by the thickness of C and Be window. For confirmation, the GEANT4 calculation values were compared with the PENELOPE Monte Carlo code [51] results and both results shows good agreement with each other (Figure 3.6). These simulations were performed with 0.5 mm thick C window and 5 mm crystal with 100 nm dead layer but without adding any Be window in the geometric model. In addition, two set of simulations were performed using pencil and isotropic beam for the cross validation of the detector efficiency calculations. In both methods, the detector efficiency calculations shows good agreement with each other (see in Figure 3.7).

The experimental and simulated absolute efficiency responses are plotted as a function of energy

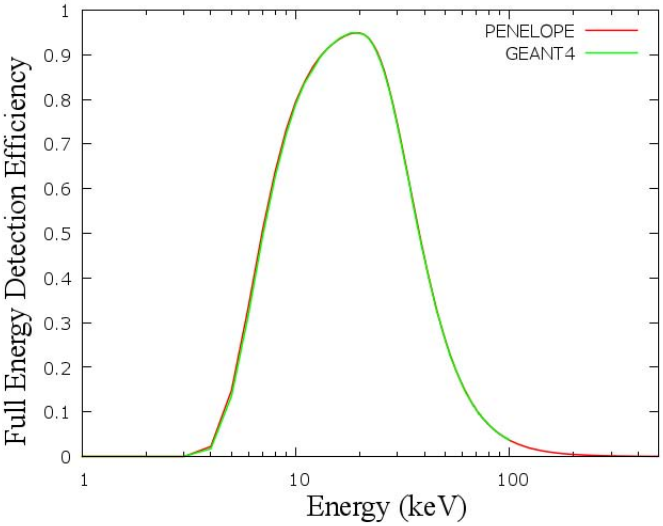

Figure 3.6: A comparison of the simulated intrinsic full energy photopeak effciencies for a Si(Li) detector with different Monte-Carlo software package. GEANT4 and PENELOPE software packages were used to perform these simulations.

for a Si(Li) detector in Figure 3.8. This comparison shows good agreement between simulation and measurements. The experimental data were acquired using multiple γ-ray photopeaks from ^{241}Am, ^{133}Ba and ^{152}Eu radioactive calibration sources when the Si(Li) detector not mounted around the trap. For measurements, the Si(Li) detector was placed on the TITAN platform and the source was located 14 cm away from detector's C window. The efficiencies from different sources were determined using the activity method [20]. The area of the peaks in the spectra and known activities of the calibrated sources were used to calculate efficiency. The activity of the source during the measurement can be calculated by Eq. 3.5:

$$A(t) = A(t_0)e^{-(t-t_0)/\tau} \tag{3.5}$$

where $A(t_0)$ is the source activity reported at $t = t_0$ by the manufacturer of the radioactive source, $(t - t_0)$ is the time elapsed since t_0 and τ is the lifetime of the source. Since the branching ratios of γ-ray sources used for these measurements are well known, absolute efficiency can be measured with a high degree of accuracy. However, the accuracy of the measured efficiency is defined by the accuracy of the calibration of the source.

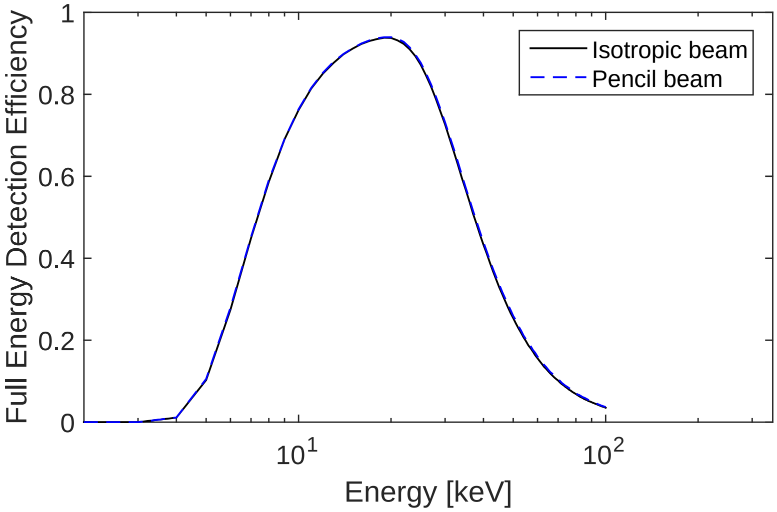

Figure 3.7: A comparison of the GEANT4 simulated intrinsic full energy photopeak efficiencies for a Si(Li) detector using pencil beam and isotropic beam.

3.2.6 Geometric Acceptance

The knowledge of solid angle efficiency of individual access ports are important to predict total experimental data taking time for ECBR measurements. As mentioned in section 2.3, the EBIT central drift tube electrode-housing cylinder has slits to access the center of the trap. Because of differing the slit size, it has different solid angle acceptance in diagonal (6-inch) and side (8-inch) access ports. To investigate this aspect, two sets of simulations were performed. Geometric arrangement for solid angle acceptance simulation is presented in Figure 3.9. In this arrangement one Si(Li) detector is rotated by 45° and placed in the opening of 6-inch access port, and another detector is placed at the opening of the 8-inch access port. For this geometric acceptance simulation, a standard isotropic ^{133}Ba source was used in the trap center. For the first simulation case, a point like source was placed at the trap center which was isotropically emitting γ-rays, and the decay events were observed and detected using both detectors. The total number of detected events were almost identical in both detectors regardless of different access ports size (presented in Figure 3.10 left). The second simulation case represents the real experimental scenario. In the TITAN EBIT, the trapped ion cloud can spread up to the full 70 mm length of the trap. For the second case an 70 mm spread out cylindrical shape source along the beam axis was used. A three dimensional vector (p_x, p_y, p_z) represents the particles gun position (ion cloud distribution) in GEANT4. For this realistic ion cloud

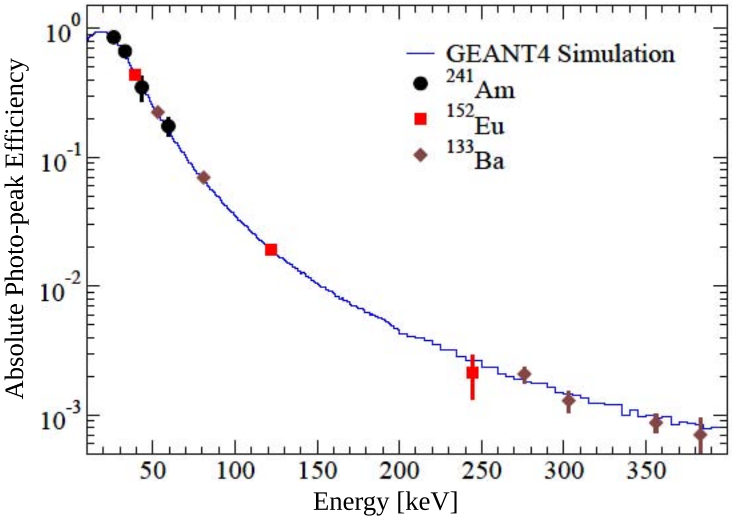

Figure 3.8: The experimental and simulated absolute efficiency responses are plotted as a function of energy for a typical Si(Li) detector. The experimental data were acquired using three different radioactive calibration sources placing 14 cm away from the detector's front C window, and the Si(Li) detector placed in the TITAN platform. (Reprinted from Ref. [40].)

distribution there was approximately a factor of 2 loss of counts for the 6-inch port compared to 8-inch port (in Figure 3.10 right). This limitation is mainly caused by geometric configuration of electrode housing and superconducting coil holder structure around the EBIT trap.

3.2.7 The Impact of the Passive Shielding on γ Background

The TITAN-EC facility was designed to observe low energy x-rays in a reduced background environment for determining weak ECBR. For the ECBR project, the region of interest in the photon spectrum is below 100 keV. However, significant background is created by Compton scattering events in that energy range. One of the most effective ways to reduce this background through active suppression of events detected in heavy material such as bismuth germanium oxide (BGO) placed around the photon detectors. In addition, passive shielding is a effective method to reduce the ambient background. A GEANT4 analysis using this geometry is ongoing at TRIUMF. For future active suppression analyses, a 1 cm thick segmented BGO crystal is placed around the Si(Li) detector, as in Figure 3.11; details about this analysis can be found in Ref. [52].

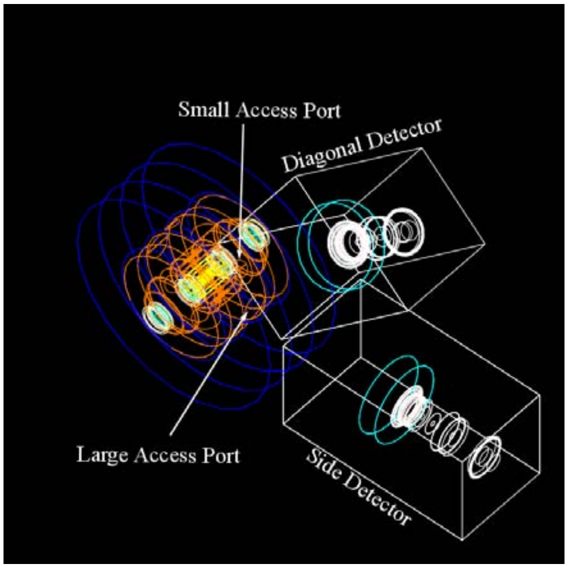

Figure 3.9: A simplified visualization of the experimental setup for detector's acceptance simulation. One detector is rotated by 45° from the reference point and placed diagonally to the EBIT trap facing the opening of the 6-inch access port. The other detector is rotated by 90° and placed on the side of the EBIT trap facing the opening of the 8-inch access port.

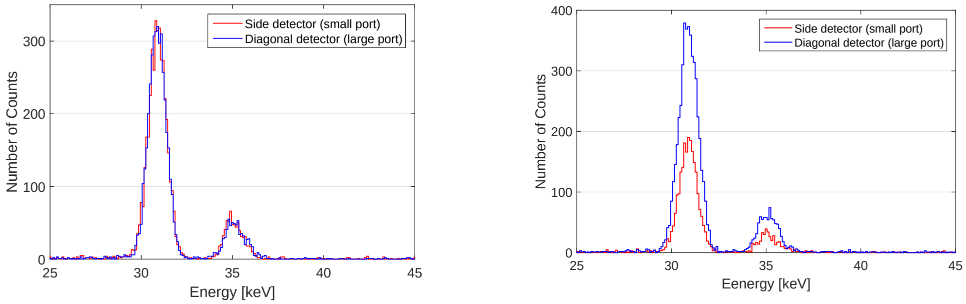

Figure 3.10: Left: A point like isotropic source at the trap center have almost identical geometric acceptance on all the access ports. Right: Realistic ion cloud distribution covering the full 70 mm trap length has approximately factor of 2 geometric acceptance loss of counts in 6-inch ports compare to large 8-inch ports.

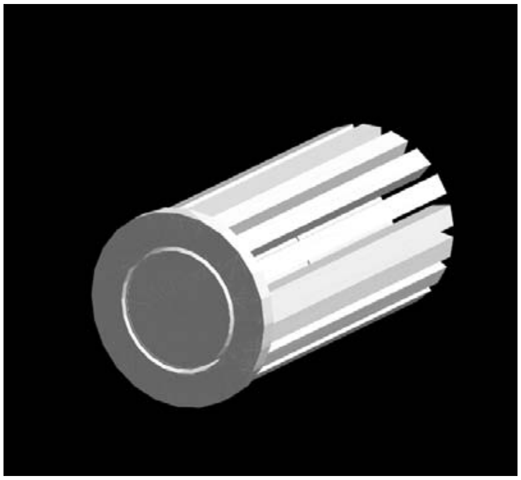

Figure 3.11: A GEANT4 model of Si(Li) detector surrounded by segmented Bismuth Germanium Oxide (BGO) shielding with Tungsten front support structure for active Compton suppression.

In addition, on going active suppression studies, passive shielding was placed around the TITAN-EC Si(Li) detectors to reduce the background. This passive shielding will reduce the ambient background and in-trap background. Due to space constraints between the Si(Li) detectors and the detector support structure only a 1 mm thick low activity Pb and a 2 mm thick Cu shield were used as passive shielding. The Cu layer is placed in a sandwich between the detector crystal and the Pb layer to block the Pb activated x-rays which may find the way to crystal. To simulate the effectiveness of passive shielding, simulation of in-trap decay spectroscopy of ^{110}Ag 1^{+} state was performed in GEANT4. For these simulations 10^{7} decay events were used. For the decay events a particle gun was placed at the center of the trap, which was modeled as a point source and decays were observed using the mounted Si(Li) detectors. In these simulations the approximation of the observed background was created in GEANT4 with and without applying the passive Cu-Pb shielding. The resulted Si(Li) energy spectra from these simulations are presented in Figure 3.12. These simulation results in Figure 3.12 show around 2 fold reduction in the background in the blue spectrum with Pb-Cu shielding.

3.2.8 The Effect of Electromagnetic Field on Background

The key advantage of the TITAN-EC experimental setup over the conventional technique is the spatial separation of the β decay electrons from the detectors, providing a reduced background environment for measuring ECBRs. In ECBR measurements, EBIT is used as a spectroscopy Penning

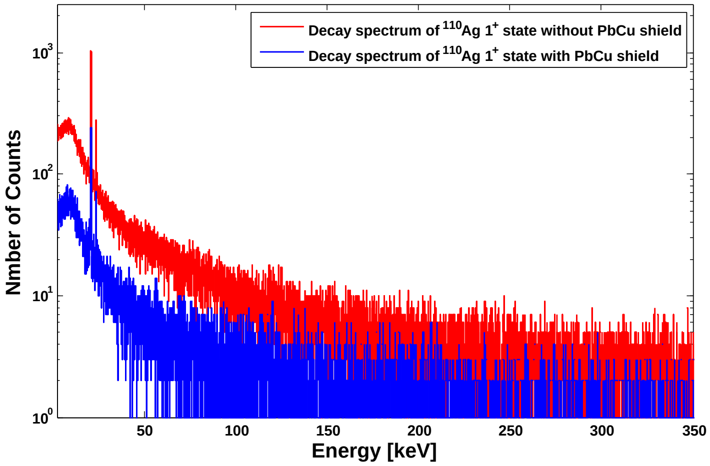

Figure 3.12: Simulations of the decay spectra of ^{110}Ag with passive Pb-Cu shielding (blue spectrum) and without passive Pb-Cu shielding (red spectrum) around the Si(Li) detectors. A 2 fold reduction in the background is observed in the simulated blue spectrum with Pb-Cu shielding.

trap, where the electrons from β-decay will be confined by the strong magnetic field. To simulate this key feature and to observe the impact of magnetic field on background, a simulation was performed by applying magnetic field in the range of 0-3 T. The ^{110}Ag ground state decay scheme was used for the particle gun source. Particles were emitted isotropically from the trap center and that time uniform magnetic field was in line with the beam axis. The red spectrum in Figure 3.13 is obtained without a magnetic field, and shows an intense β background impeding the observation of low-energy x-rays. The blue and green spectra are obtained by applying 0.5 T and 3 T uniform magnetic fields, respectively, guiding electrons out of the trap. The results show that the applied magnetic field generated a favorable environment for x-ray observation following the EC. Hence, these simulations show TITAN-EC apparatus will provide a low background environment allowing for the weak ECBR measurements.

3.2.9 TITAN-EC with Si(Li) and High Purity Germanium (HPGe) Detectors

As mentioned in section 3.2.4, the Si(Li) detectors have a maximum photon detection efficiency of 93.4% at 20 keV and it drops dramatically around 30 keV, limiting the range of possible experiments. It is possible to increase the versatility and experimental capability of in trap decay spectroscopy with the TITAN setup by using combination of Si(Li) and HPGe detectors [40]. One of the recent

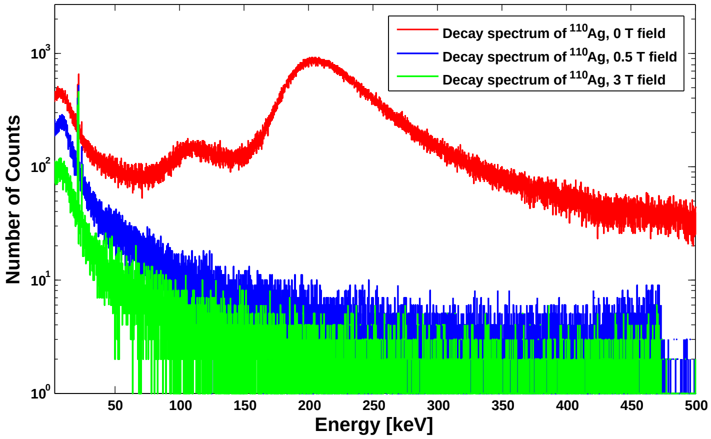

Figure 3.13: The influence of magnetic field on β and x-ray spatial separation in ^{110}Ag decay processes. The red spectrum is obtained without applying any magnetic field, showing an intense β background impeding the observation of low-energy x-rays. The blue and green spectra are obtained by applying 0.5 T and 3 T magnetic fields, respectively, that guide the electrons outside the trap, and allowing for the observation of low-energy photons.

opportunities arrived by the decommissioning program of the a high-purity germanium spectrometer (called 8π) at TRIUMF. The detectors were relocated at the Simon Fraser University for the use of nuclear science groups, and are compatible in size with the ports around the existing EBIT structure. It is possible to replace some Si(Li) detectors with the HPGe detectors around the EBIT for future experiments.

The HPGe detectors consist of cylindrical shape Ge crystals with a diameter of 50 mm and a length of 6 cm. The front face of the HPGe crystal has a 2.5 μm thick dead layer. Each crystal has a dedicated LN_2 cooled cryostat, which is heat- and vacuum-shielded by a 1.27 mm thick Be window at the front face [40]. Each HPGe detector is equipped with BGO shielding around the crystal for active Compton suppression. However, the HPGe detectors with BGO shielding configuration cannot be used around the trap due to space constraints but it can be removed. Based on the dimensions obtained from technical drawing of HPGe detector, a GEANT4 model of HPGe was developed. The resolution function for HPGe detector was extracted from standard source data and embedded in GEANT4 code. The GEANT4 simulated model of the combination of HPGe and Si(Li) detectors around the EBIT is represented in Figure 3.14. A cross section of these detectors and EBIT system are presented in Figure 3.15. For future experiments it is planned to place 3 HPGe detectors in the

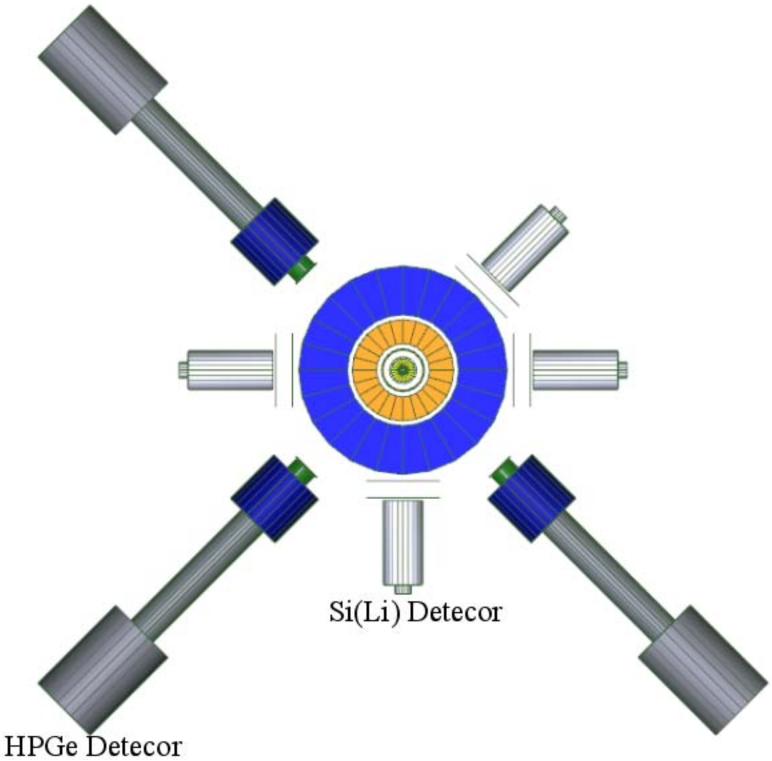

Figure 3.14: Visualization of the simulated geometry of the TITAN-EC experimental setup with combination of Si(Li) and HPGe detectors around the trap. Three HPGe detectors from TRIUMF's γ-ray spectrometer are located at diagonal positions facing 6-inch access ports, and Si(Li) detectors are located at side positions facing 8-inch access ports.

6-inch small ports without losing too much solid angle acceptance for Si(Li) detectors.

The comparison of the absolute intrinsic photon detection efficiency of HPGe and Si(Li) detector is displayed in Figure 3.16. These HPGe and Si(Li) detectors have identical efficiency below 20 keV. However, at low energy the efficiency curve is limited by the thickness of the detectors built-in C and Be windows. Above 20 keV the HPGe crystals can gain a large increase in efficiency because of crystal thickness, which can help to make the future TITAN experiments versatile. Similar to Si(Li) detector efficiency simulations, these simulations were performed in the energy range from 1 keV to 1000 keV with 1 keV steps and 10^6 monoenergetic γ-rays were used for each energy. For these simulations, γ-rays were fired from a point source towards the center of the HPGe crystal.

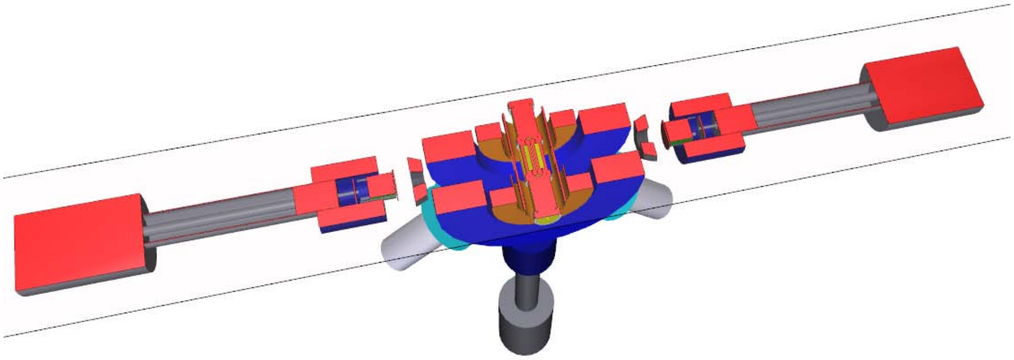

Figure 3.15: Visualization of the simulated geometry of TITAN-EC experimental setup with combination of Si(Li) and HPGe detectors around the trap. Three HPGe detectors and one Si(Li) detector are located at diagonal positions facing the 6-inch access ports, and three Si(Li) detectors are located at side positions facing 8-inch access ports.

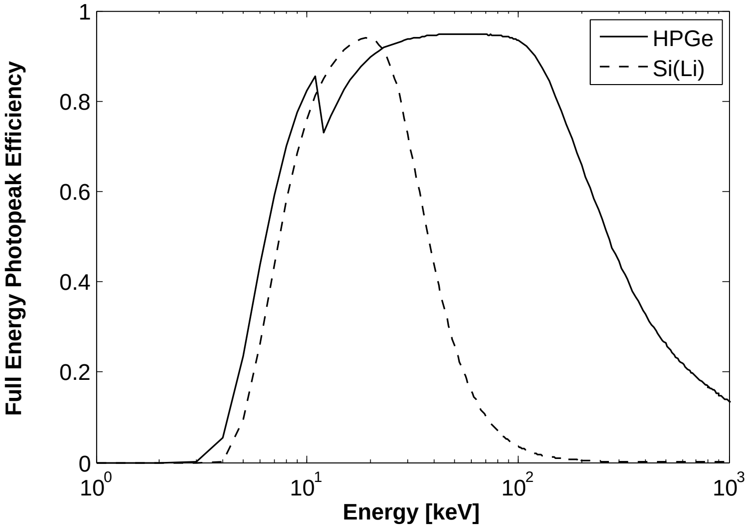

Figure 3.16: A comparison of the simulated intrinsic efficiencies for a Si(Li) detector and a HPGe detector. The efficiency profiles are nearly identical below 20 keV, but a large increase in detection efficiency above 20 keV can be gained using the HPGe detector. The low-energy response of the respective curves is determined by the thickness of the Be and C front-face windows on the HPGe and Si(Li) detectors, respectively.

Chapter 4

Comparison of GEANT4 Simulation and Experimental Data

In chapter 3, the development of TITAN-EC simulation process, systematic studies of TITAN-EC detector efficiency simulation and validation, solid angle acceptance calculation, the impact of passive shielding on background measurement and the main key feature of the TITAN-EC's magnetic field effect on spatial separation of x-ray from β background were presented. In this chapter, using the detector efficiency and the experimental apparatus model, predictions for the performance of the TITAN-EC simulation will be presented by comparing with experimental results. This prediction will help researchers to estimate the TITAN-EC apparatus performance for designing future experiments. Additionally, these predictions will help to understand the uncertainties associated with the design of experiments to effectively estimate required beam time for future experiments.

For the commissioning of the TITAN-EC decay-spectroscopy apparatus, an experiment was performed with a ^{124}Cs radioactive beam [53]. The objective of this experiment was to investigate the TITAN-EC array with an on-line radioactive beam and characterize the experimental apparatus by observing EC decays of ^{124}Cs. Radioactive isotope of ^{124}Cs was chosen because of its large EC branch of 7% and short half-life of 30.8 s, which are both well known and therefore suited to providing a benchmark test [53]. To investigate the performance of the developed Monte-Carlo simulation prediction power, simulations were performed with experimental conditions of this commissioning experiment. The beam delivered from the TRIUMF ISAC facility was produced by bombarding a uranium carbide (UC_2) target with a 480 MeV, 9.8 μA proton beam. The beam was composed

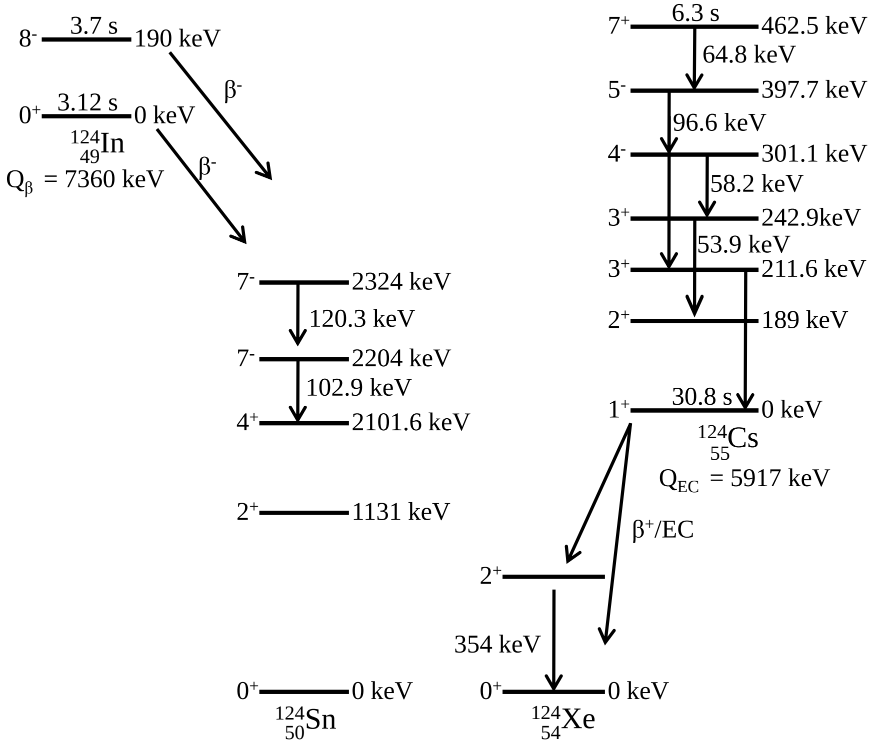

Figure 4.1: The partial decay scheme of ^{124}Cs and ^{124}In and their isomers (^{124}Cs $J^{\pi} = 7^{+}$ and ^{124}In $J^{\pi} = 8^{-}$) according to the nuclear transitions recorded in [49].

of 65% ^{124}Cs $J^{\pi} = 1^{+}$ state and 3% ^{124}Cs $J^{\pi} = 7^{+}$ state with 32% (^{124}In $J^{\pi} = 1^{+}$ state and ^{124}In $J^{\pi} = 8^{-}$ state) contamination according to the yield measurement [54]. The high level of ^{124}In contamination was produced due to the use of UC_2 as production target material. This contamination was not previously detected with the Ta as production target material [55]. The partial decay scheme of ^{124}Cs,^{124}In and their isomers according to the nuclear transitions recorded in [49] are presented in Figure 4.1.

The radioactive ions were cooled and bunched at the TITAN-RFQ for 1 s, then tuned for mass A = 124 and transported into the EBIT using a transport potential of 1 kV. A total of 30 s trapping cycle, consisting of 25 s decay measurement and of 5 s empty trap background measurement cycle was used for approximately 48 hrs of data recording. The trapping potential of the EBIT was lifted to empty the trap before each background measurements, the trap loading and emptying was performed on a submillisecond time scale [40].

Simulated photon spectra from 10 keV to 160 keV of ^{124}Cs for the commissioning experiment using the full TITAN trap geometry are presented in Figure 4.2. To simulate the ^{124}Cs photon decay spectrum, two individual simulations for the ^{124}Cs $J^{\pi} = 1^{+}$ ground state and ^{124}Cs $J^{\pi} = 7^{+}$ isomeric state were performed and combined. For each case, 20×10^{6} and 4×10^{6} isotropic decay events were used from the TITAN-EC trap center, to generate these individual decay spectra (in Figure 4.2 green spectrum for ^{124}Cs $J^{\pi} = 1^{+}$ ground state and blue spectrum for ^{124}Cs $J^{\pi} = 7^{+}$ isomeric state). For the decay process of $^{124\text{g,m}}$Cs, all known x-ray and γ-ray transitions are included in the simulation input file according to Ref. [49]. The Si(Li) detector energy resolution function was extracted by fitting the experimental data and included in the GEANT4 simulation for deposited energy in detector crystals to make the simulation spectra realistic and comparable with experimental data.

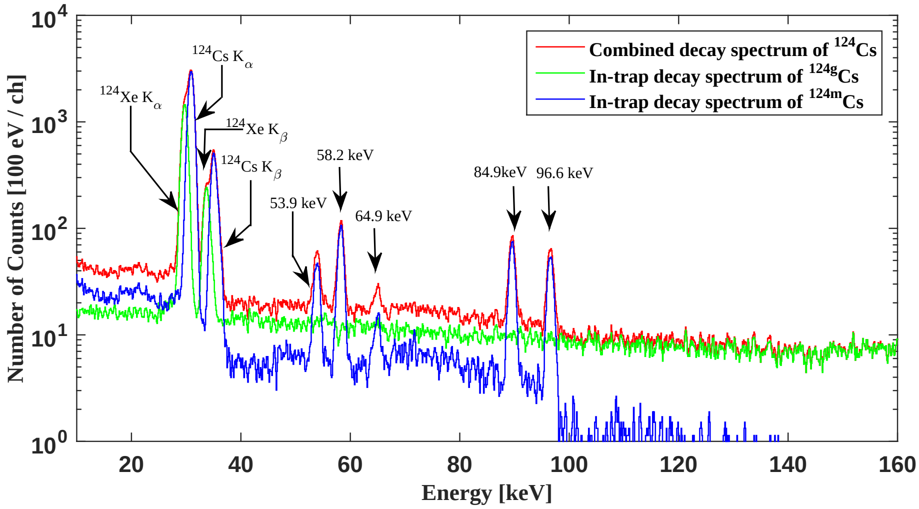

Figure 4.2: Simulated photon spectra from 10 keV to 160 keV for commissioning experiment [53] using full trap geometry. The simulated spectra result from the same number of events from commissioning experiment and show the nuclear transitions from $^{124\text{m}}$Cs (blue spectrum), $^{124\text{g}}$Cs (green spectrum) and combined ^{124}Cs (red spectrum) decays.

As mentioned in an earlier paragraph, a contamination of 32% of ^{124}In $J^{\pi} = 1^{+}$ ground state ($T_{1/2} = 3.12$ s) and ^{124}In $J^{\pi} = 8^{-}$ isomeric state ($T_{1/2} = 3.7$ s) has been observed and measured in the beam. To simulate the significance of contamination on ECBR measurement, 2.5×10^{8} and 2.5×10^{7} decay events for ^{124}In $J^{\pi} = 1^{+}$ ground state and ^{124}In $J^{\pi} = 8^{-}$ isomeric state were simulated, respectively, in 4π radians from the trap center. Similarly, ^{124}Cs decay simulation, all known x-ray

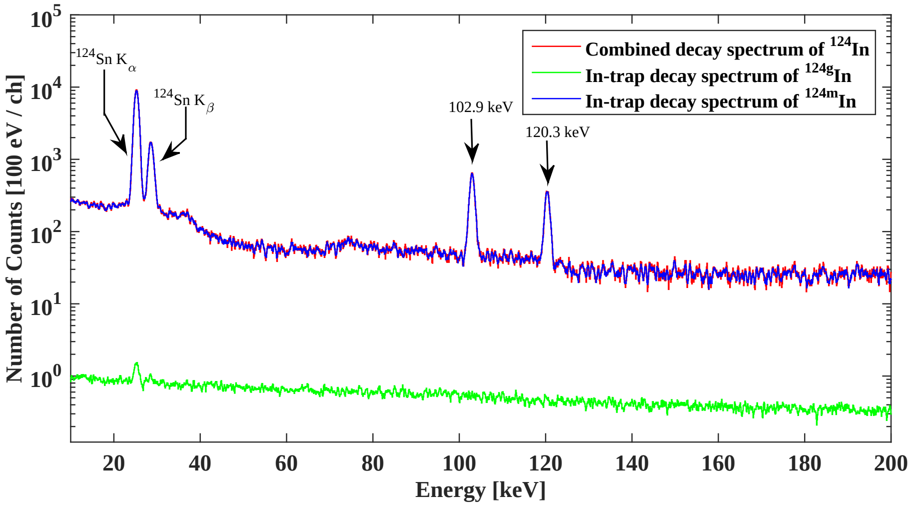

Figure 4.3: Simulated photon spectra from 10 keV to 200 keV for commissioning experiment [53] using full trap geometry. The simulated spectra result from same number of events from commissioning experiment and show the nuclear transitions from ^{124m}In (blue spectrum), ^{124g}In (green spectrum) and combined ^{124}In (red spectrum) decays.

and γ transitions were included in simulation input file according to Ref. [49]. GEANT4 simulations of photon spectra are shown in Figure 4.3 for the ^{124}In $J^\pi = 1^+$ ground state (green spectrum) and the ^{124}In $J^\pi = 8^-$ isomeric state (blue spectrum), and combined decays (red spectrum).

In Figure 4.4(a) the red spectrum shows the combined decay spectrum from energy 10 keV to 160 keV of ^{124g,m}In and ^{124g,m}Cs decay scheme of the commissioning experiment. Also in Figure 4.4(a) the blue and green spectra are showing the contribution of (^{124g,m}Cs and ^{124g,m}In) species in the final decay spectrum. Figure 4.4(b) highlights the x-ray energy region ranging from 20 keV to 42 keV, which energy range is the region of interest for the ECBR measurement experiment. In the combined spectrum k_α and k_β x-ray peaks are visible from these isobars, i.e., ^{124}Cs [from internal conversion (IC) of ^{124m}Cs], ^{124}Cs [from ^{124}Cs EC ground state decay] and ^{124}Sn [from IC following ^{124m}In β^- decay] and highlighted in the in Figure 4.4(b). In addition to these x-ray peaks, γ-rays at 53.9 keV, 58.2 keV, 89.5 keV and 96.6 keV from ^{124m}Cs isomer decay and γ-ray transitions at 102.9 keV and 120.3 keV from ^{124m}In isomer are also visible in Figure 4.4(a).

A simulated three-dimensional view of energy-time photon decay spectrum of the 20 keV to 40 keV x-ray region for the commissioning experiment is shown in Figure 4.5. The time for each decay

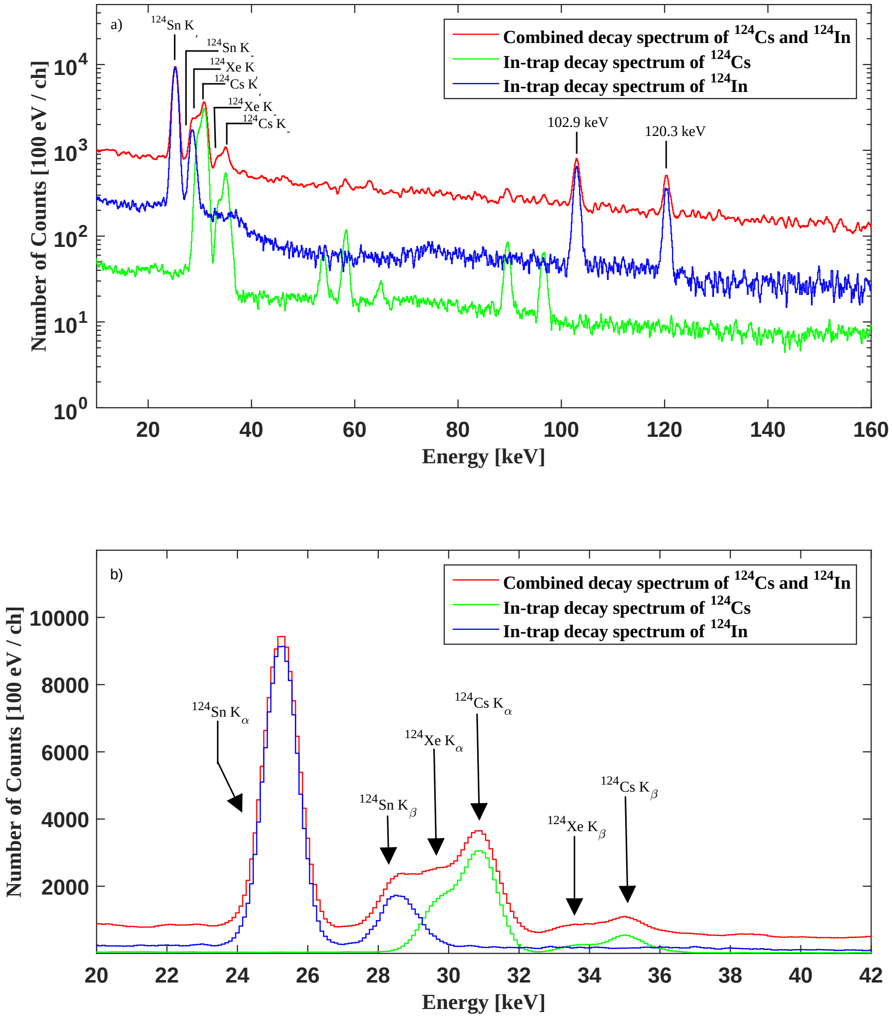

Figure 4.4: a) Simulated photon spectra from 10 keV to 160 keV for the commissioning experiment [53] using the full trap geometry. b) Displays the energy region 20-42 keV highlighting the x-ray region. The simulated spectra result from same number of events from commissioning experiment and show the nuclear transition from ^{124g,m}In (blue spectrum), ^{124g,m}Cs (green spectrum) and combined ^{124}Cs and ^{124}In (red spectrum) decays.

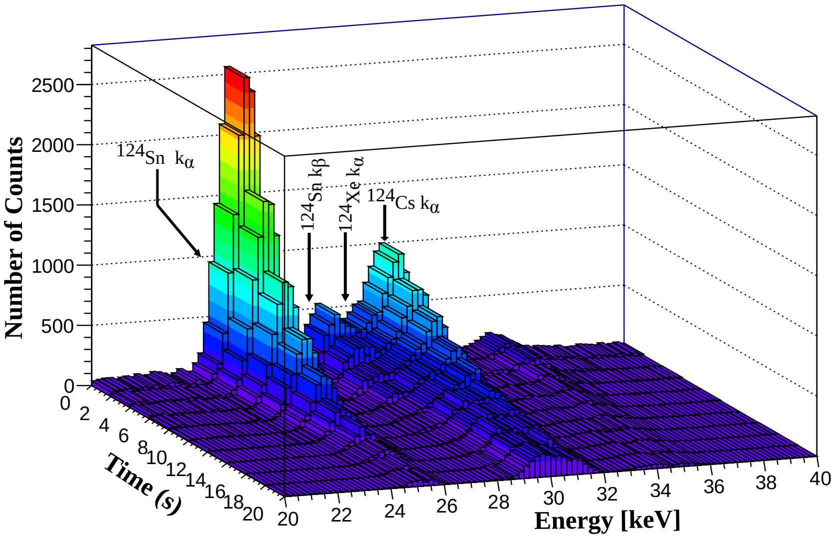

Figure 4.5: Photon energy-time matrix from 20 keV to 40 keV, highlighting the x-ray region for the commissioning experiment [53] using the TITAN-EC full trap geometry. The curve shows nuclear transition from ^{124g,m}Cs with ^{124g,m}In contamination, where they have characteristic half lives of 30.8 s and 3.12 s, respectively.

event for ^{124}In and ^{124}Cs decay experiment was generated using Monte Carlo method for sampling from an exponential distribution based on individual species half-life. Time interval is calculated using the formula:

$$\Delta t = \frac{-1}{\lambda} ln(1-R) \tag{4.1}$$

where, R is the uniform random number distribution between 0 to 1 and λ is the decay constant. ^{124}Cs and ^{124}In have characteristic half-lives of 30.8 s and 3.12 s respectively, which is also visible in the decay 3-D spectrum. This timing information also helps to identify the radioactive isobars based on half-life of the components. Figure 4.6 also shows that the short lived components (^{124m}In and ^{124m}Cs) will disappear after certain time and will successively enhance the detection of signature x-rays from 30.8 s ^{124m}Cs EC decays.

The simulated spectra for the four species (^{124g,m}In and ^{124g,m}Cs) presented in Figure 4.2-4.5 are compared with experimental data and their differences minimized towards a certain set of parameters. Minimization is performed by least-squares method of simulated spectrum to the measured spectrum, taking into account the statistical uncertainties. For this minimization analysis, a Python optimization library was used. The Python optimization library uses the Levenburg-Marquardt algorithm to minimize the objective function. Details about this minimization process is presented in Appendix D.

The comparison between simulated and experimental spectra from the energy range 10 keV to 200 keV is presented in Figure 4.6(a). Figure 4.6(b) shows the comparison of spectra for x-ray region energy ranging from 20 keV to 42 keV, which is the region of interest for ECBR measurement. The minimization of the sum of residual uses 5 parameters, 4 as the normalization factor for the four simulated species and 5^{th} one for the background scaling. The high-statistics background data is taken from the commissioning experiment and used in the analysis. As a result of the minimization of the differences between the simulated data to the experimental data, A_1, A_2, A_3, A_4 and A_5 coefficient for normalization and background scaling values and statistical uncertainties are shown in Table 4.1.

Table 4.1: Fit parameter values and related uncertainties from the least-squares minimization of simulated data to experimental data

Description	Coefficient	Fixed/Free	Value	Statistical Uncertainties
Normalization Factor for ^{124g}Cs	A_1	Free	0.3695	0.0007
Normalization Factor for ^{124m}Cs	A_2	Free	0.5678	0.0002
Normalization Factor for ^{124g}In	A_3	Free	0.0126	0.0003
Normalization Factor for ^{124m}In	A_4	Free	3.0879	0.0026
Scaling Factor for Background	A_5	Free	0.9322	0.0021

The residual of the least square minimization for simulated spectra to measured spectra is presented in Figure 4.6(c). This analysis provides good agreement for energies of several hundred keV between simulation and experiment with regard to the overall shape of the background. Small discrepancy between simulation and experiment may be caused by performing charge breeding on trapped radioactive ions in the experiment and which is not implemented in simulation. For charge breeding, the trapped ions were bombarded with a continuous 85 mA electron beam. As result of these charge-bred, highly charged ions will show a change in the binding energies for the innermost electrons resulting a shift in k_α and k_β x-ray energy. Details about highly charged ions trapping and their impact on x-ray energy shift can be found in Ref. [53].

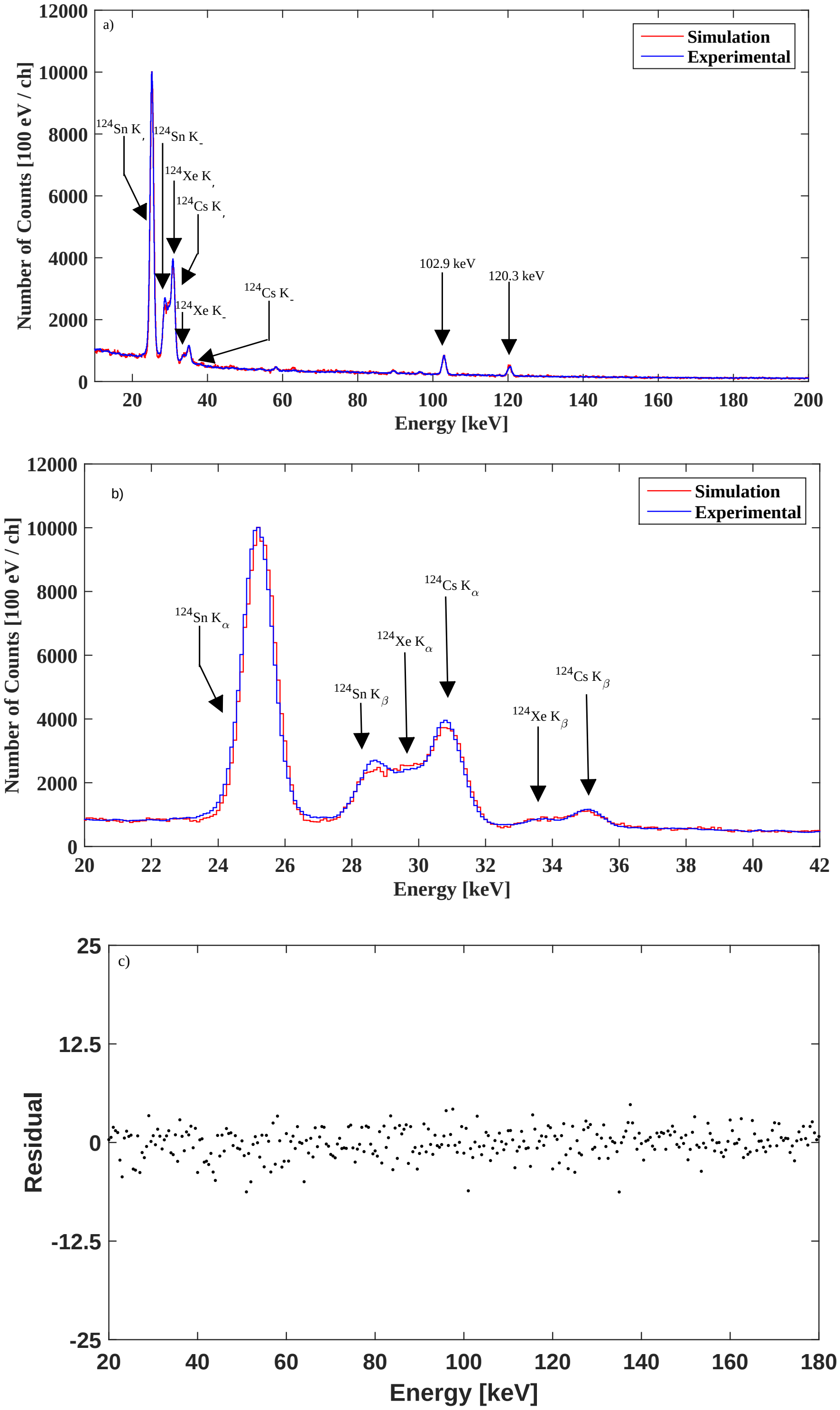

Figure 4.6: a) The comparison between experimental (blue spectrum) and simulated (red spectrum) spectra from 10 keV to 200 keV for the (^{124g,m}Cs and ^{124g,m}In) commissioning experiment [53] using full trap geometry. b) the x-ray region from 20 keV to 42 keV, and c) residual for the least square minimization for simulated spectra to measured spectra.

Chapter 5

Annealing Station

As mentioned in section 3.2.9, the 8π spectrometer consisting of 20 Compton-suppressed HPGe detectors has been decommission at TRIUMF and relocated to SFU. Up to 7 of these HPGe detectors could be used in in-trap spectroscopy experiments with TITAN at TRIUMF. These germanium detectors will be used to detect γ-rays produced from a wide range of experiments using radioactive ion beams and radioactive decays. In some experiments, these HPGe detectors will be exposed to neutron interactions that will result displacement of atoms in detector crystal structure. These damages can change the average drift velocity of electrons and holes, leading to low energy tails on the photo peaks, which degrades the energy resolution of the detectors and increases the leakage current of detector. However, these kind of damages can be successfully repaired by annealing (heating up the crystal of detector). The development of the annealing station and annealing process of a typical HPGe detector are described in this section. For annealing and recovering of the energy resolution of a HPGe detector, the detector crystal needs to be heated at $\approx 80°\text{C}$ for 12-24 hr. Before starting the heating process, the detector's chamber needs to be pumped out to a pressure of $\approx 10^{-6}$ torr and maintain this pressure until detector crystal reach room temperature after heating.

Figure 5.1 represents the schematic diagram of annealing station showing the main components. Two pumps (a rough pump and a Varian 941-6501 sorption pump) are used in the system to obtain the high vacuum (HV) pumping pressure of 10^{-6} torr. The pumps are connected to a three-way tee through two Edwads SP25 diaphragm sealed in-line isolation valve. These valves allow the user to separate sorption and rough pump from the rest of the vacuum system. This tee is mounted on a four-way cross through another SP25 diaphragm sealed in-line isolation valve, which allows the user to separate the detector crystal section from the pumping sections. A photograph of the

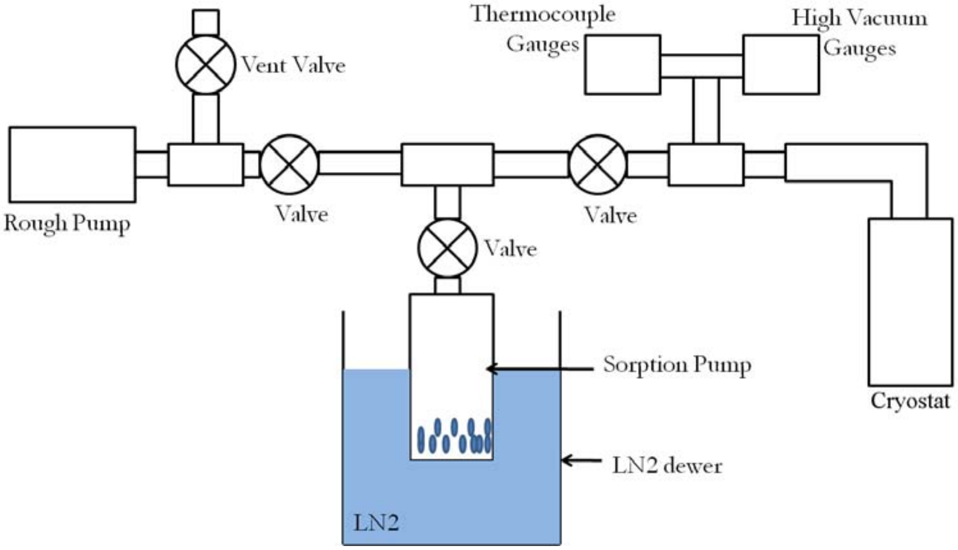

Figure 5.1: Schematic diagram of the annealing station showing its main components.

annealing station is shown in Figure 5.2(a), and the arrangement of the vacuum valves and vacuum components are shown in Figure 5.2 (b) and (c). A thermocouple gauge (Varian TC 536) and a high vacuum gauge (Varian IMG 100) are mounted on the two end of the cross to monitor the pressure at the detector end. The other end of the cross is connected to a converter that connects the detector's vacuum chamber port to vacuum system. To seal the connection between vacuum parts, O-rings and copper gaskets were used.

Sorption pumps work according to the principle of adsorption of gases at the very large surfaces of molecular sieves by cooling the sieve materials below the boiling point of most gases. Here gas molecules strike this sticky cooled micro-porous surface become attached and effectively pumped off from the vacuum system. For the sorption pump, one gallon zeolite (MS-5A-23, alkali alumino-silicate) from Duniway was used as sieve material, which processes a very large surface area about 1000 m^2/g of solid substance. Pore diameter of zeolite 13X is about 10^{-10} m which is appropriate for capture of the gases most predominant in the atmosphere. After pouring the sieve materials in the pump, a conical screen was installed at pump opening to protect molecular sieve materials from leaving the sorption pump. The sorption pump was selected for annealing station due to clean and vibration free operating environment. This pump do not require any oil to operate, which allows the vacuum system to be clean from any accidental backstreaming of oil from the sorption pumps to the rest of the HV system. Besides, sorption pump is inexpensive and easy to maintain, with no mechanical failure.

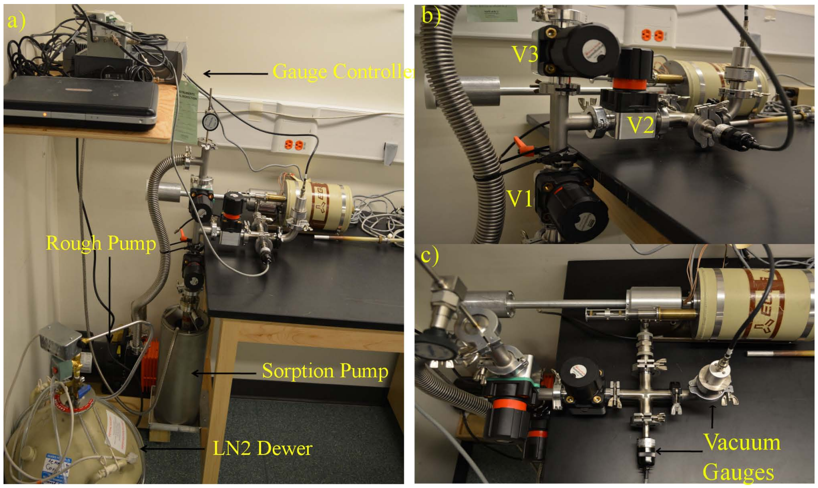

Figure 5.2: a) A photograph of the HPGe detector pumping/toasting station in the nuclear science laboratory at SFU, showing sorption pump, roughing pump, LN_2 dewer, pressure gauges and control system modules. b) Valves V_1, V_2 and V_3 are used to disconnect the sorption pump, cryostat and rough pump from main setup frame, respectively. c) A HPGe detector is connected to annealing station for pumping down and backing. Vacuum gauges are used to monitor the pressure at the inlet port of the detector.

To start the adsorption process, sieve materials were cooled at liquid nitrogen (LN_2) temperature by pouring LN_2 in the sorption pump dewer and this dewer needs to be refilled every 4 hr throughout the operation of sorption pump. This LN_2 filling is automatically controlled by using a National Instrument (NI) USB 6008 data acquisition (DAQ) system, custom made relay drive circuit and LED based overflow sensor.

Following repeated use of the sorption pump, molecular sieve inside the sorption pump will be saturated with gas molecules. At this condition the pump's ability to remove the gas from the vacuum system will be deteriorate rapidly. In this condition, regeneration of the molecular sieve is necessary to maintain normal operating condition. To perform the regeneration steps, the sortion pump needs to be valved off from the vacuum system and allowing the pump to reach room temperature. The sorption pump's wrap-around heater needs to be turned on to bake out the sieve materials at 250°C for 12 hr. This process will lead the sieve materials to outgas absorbed gases and these gases will be pumped out using roughing pump.

For the annealing process of the HPGe detector, the following process needs to be carried out as follows:

1. The detector is allowed to warm up to room temperature,
2. Roughing pump is used to pump out the air from inside of the vacuum chamber to achieve a pressure of 10^{-4} torr and sorption pump to achieve a pressure of 10^{-6} torr,
3. Separate the sorption pump from the rest of the vacuum system,
4. Place LN_2 in sorption pump dewer around the pump and periodic refill of LN_2 is necessary,
5. Allow sorption pump to chill for 10 min or longer so the sieve material will be near LN_2 temperature,
6. Separate the roughing line and valve on the sorption pump to reach a pressure of 10^{-6} torr,
7. Open detector valve to pump out the detector's vacuum chamber,
8. Place the resistive heating rod inside the detector and set temperature regulator to heat detector at 80°C,
9. Pump at a constant temperature of 80°C for 12 hrs,
10. Turn off heat and let the detector cool down to room temperature,
11. Close valve and disconnect vacuum pump.

A HPGe detector was annealed at 80°C for 12 hr and pressure was recorded throughout the annealing process (shown in Figure 5.3). After opening the detector valve, the pressure of the vacuum system jumped to 6.1×10^{-5} from 7.5×10^{-6} torr and gradually reached to 1×10^{-5} torr. After turning on the heating system vacuum pressure starts to deteriorate due to the materials outgassing from the detector vacuum chamber and over the time of the annealing process detector vacuum reaches the optimum pressure of normal detector operation.

To investigate the effect of annealing process on the detector energy resolution, spectra were taken with the HPGe detector before and after annealing using a ^{60}Co source and the full width half max (FWHM) of the 1332 keV photo-peak was measured. This comparasion shows 0.031% improvement in the energy resolution after the annealing process from the previous condition. The comparasion of 1332 keV photo-peak before and after annealing process is presented in Figure 5.4.

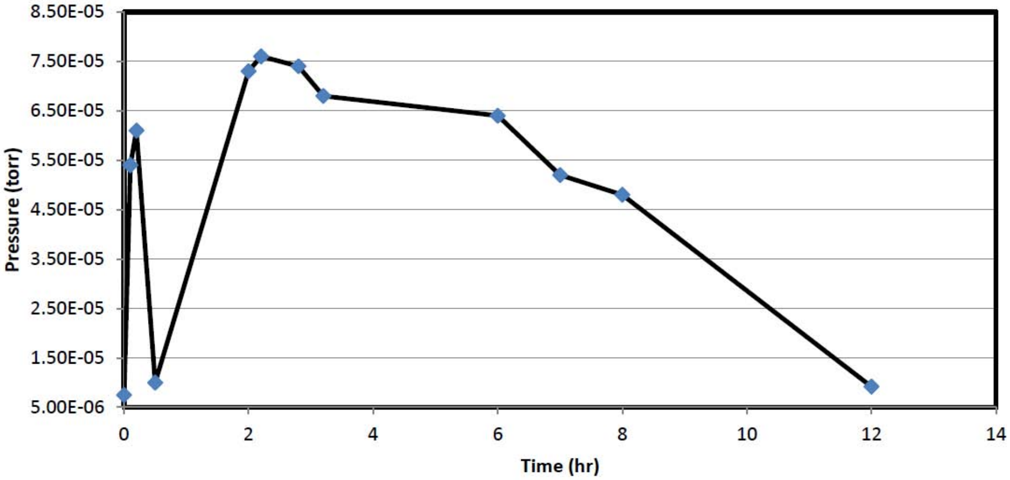

Figure 5.3: Pressure reading from HV gauge throughout the annealing process. The pressure reading at HV gauge goes up after opening the detector vacuum port or after turning on the crystal heating system due to material outgassing. Over the time of the annealing process detector vacuum reaches the optimum pressure of normal detector operation

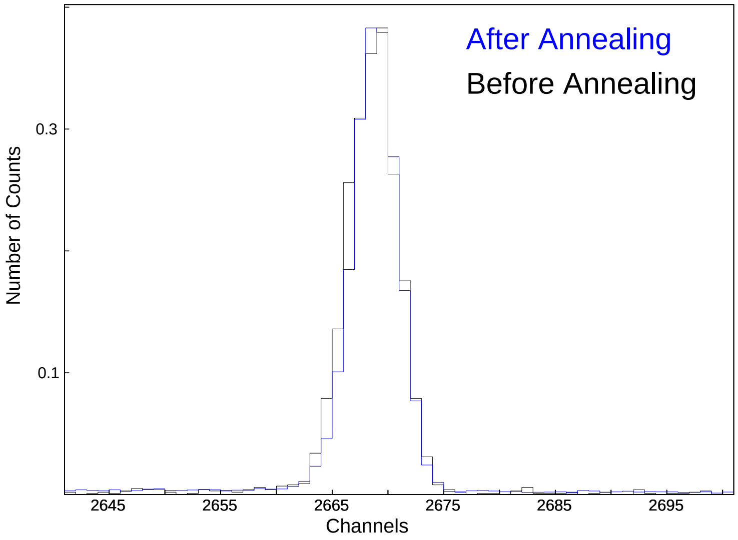

Figure 5.4: A full energy deposition, before (black spectrum) and after (blue spectrum) annealing process at 1332 keV from ^{60}Co standard calibration source.

Chapter 6

Conclusions and Future Direction

6.1 Conclusions

A comprehensive GEANT4 based simulation software package has been developed to optimize the TITAN-EC experimental set-up at TRIUMF. Using this software an extensive set of simulations has been used as predictive tool for preparing experiments as well as data analysis. The photon detection efficiency of the Si(Li) detectors of TITAN-EC decay station was successfully determined and validated by comparing with different Monte-Carlo calculations and experimental data from ^{241}Am, ^{133}Ba and ^{152}Eu standard calibration sources. Systematic studies of geometric acceptance were performed using this simulation program helping to identify the count rate difference on different access ports. This simulation also allowed for the investigation of the impact of passive shielding on background measurement and another individual investigation of active Compton suppression analysis is ongoing using this simulation package. The most important key feature of TITAN-EC experimental setup is the spatial separation of x-ray and β background by applying strong magnetic field. This key feature was also simulated using this software package by applying uniform magnetic field of different strength.

After performing extensive systematic studies of the TITAN-EC apparatus, the simulation program was used to generate realistic data for the commissioning experiment. Simulated in trap spectra of ^{124}In ($J^{\pi} = 1^{+}$ ground state and $J^{\pi} = 8^{-}$ isomeric state) and ^{124}Cs ($J^{\pi} = 1^{+}$ ground state and $J^{\pi} = 7^{+}$ isomeric state) was compared with experimental data and this comparison showed a good agreement between GEANT4 simulations and experimental data. The GEANT4 simulations described in this thesis accurately present the physics involved in ECBR experiments. The simulation software developed as part of this thesis is capable of simulating any proposed cases for ECBR measurement program at the TRIUMF. The predictive power of GEANT4 simulation will allow researchers to understand the uncertainties involved in designing future experiments. However, the background in TRIUMF experimental hall is always changing and it is a difficult task to model the background properly. The TITAN platform at ISAC experimental hall and aluminum support structure for detector needs to be included in GEANT4 geometry for a complete modeling of the radiation background. Additionally, the development of simulation program, annealing station for HPGe detector has been developed as part of this thesis. This apparatus will be used as essential part of the Neutron Generator monitoring facility located at SFU.

6.2 Future Direction

The Si(Li) detectors efficiency at high energies limits the range of experiments possible with TITAN-EC decay station. The increase in detector efficiency will provide TITAN-EC apparatus a versatile experimental capability. Besides, the normalization of ECBR calculation can be achieved by using high-energy γ line. As mentioned in section 3.2.9, after decommissioning of the 8π spectrometer consisting of 20 Compton-suppressed HPGe detectors, the HPGe detectors were relocated to SFU and will be available for future use. These detectors are 6 cm thick and have much higher efficiency at high energies. The comparison of Si(Li) and the HPGe detector's efficiency is presented in Figure 3.14. One of the possible proposals is to use 3 HPGe detectors in combination with 4 Si(Li) detectors around the TITAN's EBIT to improve the efficiency over a wide range of energies. To investigate the outcome of the proposal, the HPGe detectors were modeled in GEANT4 simulation. The commissioning experimental simulations presented in chapter 4 were performed again by placing 3 HPGe detectors are in diagonal positions and 4 Si(Li) detectors are in side positions around the EBIT. The same numbers of events mentioned in chapter 4 are used for simulation ^{124}In ($J^{\pi} = 1^{+}$ ground state and $J^{\pi} = 8^{-}$ isomeric state) and ^{124}Cs ($J^{\pi} = 1^{+}$ ground state and $J^{\pi} = 7^{+}$ isomeric state) decay processes. The comparison of simulated photon spectra using 3 HPGe and 4 Si(Li) detectors are presented in Figure 6.1. In Figure 6.1 high energy γ lines from high spin states are visible after 150 keV in HPGe detectors compared to Si(Li) detectors. However, it is also visible in these spectra that HPGe detector will see more Compton background compared to Si(Li) detectors.

Following the proposed list of nuclei that will be investigated by the TITAN-EC program, the next step will be the ECBR measurement of ^{110}Ag. In the ^{110}Pd double-β decay process, ^{110}Ag is

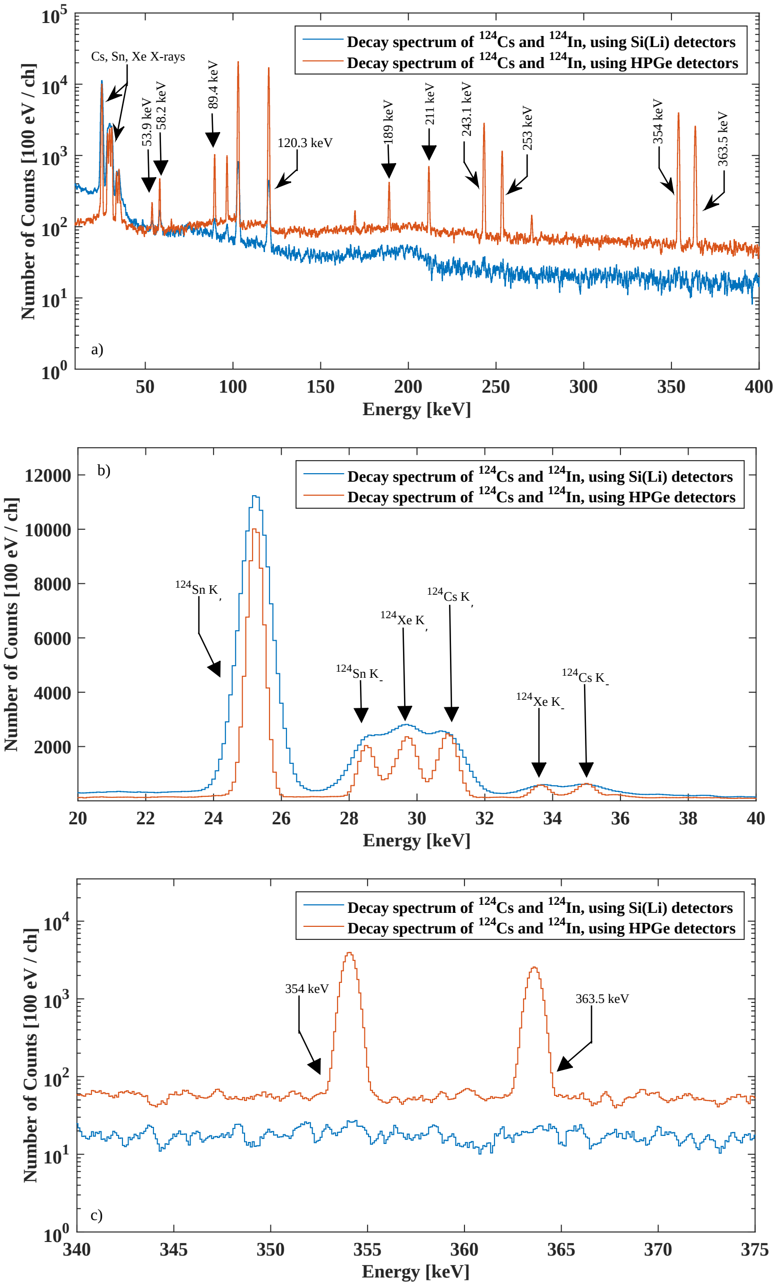

Figure 6.1: a) Top panel shows the comparison between experimental (blue spectrum) and simulated (red spectrum) spectra from 0 keV to 400 keV for the commissioning experiment [53] using ^{124g,m}Cs and ^{124g,m}In) and the full trap geometry. b) Middle panel shows the k_α and k_β x-rays from ^{124g,m}Cs and ^{124g,m}In decays in the energy range from 20 keV to 40 keV. c) The bottom panel displays full γ energy deposition peaks in energy range from 340 keV to 375 keV, highlighting in photon detection deficiencies in both detectors.

the intermediate nucleus, which can be produced with states: the $J^{\pi} = 1^{+}$ ground state ($T_{1/2}$ = 24.6 s) and $J^{\pi} = 6^{+}$ isomeric state ($T_{1/2}$ = 249.7 d). The ECBR of ^{110}Ag has been measured in 1965 using conventional techniques [56] and has a EC branching ratio of 0.3%. So, the ECBR measurement of ^{110}Ag will be a good case to investigate the limit of TITAN-EC apparatus. The partial decay scheme of ^{110}Ag is presented in appendix E.

To simulate the case of ^{110}Ag, from the trap center 50 million isotropically decay events for both ground state and isomeric state were used. This simulation was performed using TITAN-EC's full trap geometry and a combination of 4 Si(Li) (placed in front of the 8 inch ports) and 3 HPGe detectors (placed in front of the 6 inch ports) were used to detect the photons. The photon decay spectra from energy 1 keV to 1000 keV of ^{110}Ag using 4 Si(Li) detectors (blue spectrum) and 3 HPGe detectors (red spectrum) are presented in Figure 6.2(a). The important x-ray energies (21.2 keV, 22.2 keV and 23.3 keV) for ECBR measurement are presented in Figure 6.2(b). For the case of ^{110}Ag ECBR measurement, the normalization can be achieved by using 657.8 keV γ line from first 2^{+} excited state of ^{110}Cd. Due to the superior efficiency of the HPGe detector at high energies, the spectrum can be used to normalize the ECBR data using the 657.8 kV γ-ray transition. This line is not visible in the photon spectrum obtained with Si(Li) detectors (blue spectrum in Figure 6.2(c)). In addition, full width half max (FWHM) of HPGE detector is 0.475 keV at 21.1 keV, where as the FWHM of Si(Li) detector is approximately double at the same energy. In some cases it is difficult to distinguish neighboring x-ray peaks using Si(Li) detector because of resolution issue. Based on these results, it is recommended to use the HPGe detectors for the ECBR measurement program.

The GEANT4 simulation of 4 Si(Li) and 3 HPGe detectors can be used to predict the result of an experiment especially when the high energy γ line is necessary for data analysis and calibration. The verification of simulated result for the HPGe data should be made by comparing with calibration source and with the experimental data. In addition, another simulation for segmented BGO shielding for active Compton suppression is currently performed and needs to be validated with experimental data and then integrated with this software package. The ECBR program will continue this year with branching ratio measurement of ^{110}Ag and beam development of ^{100}Tc.

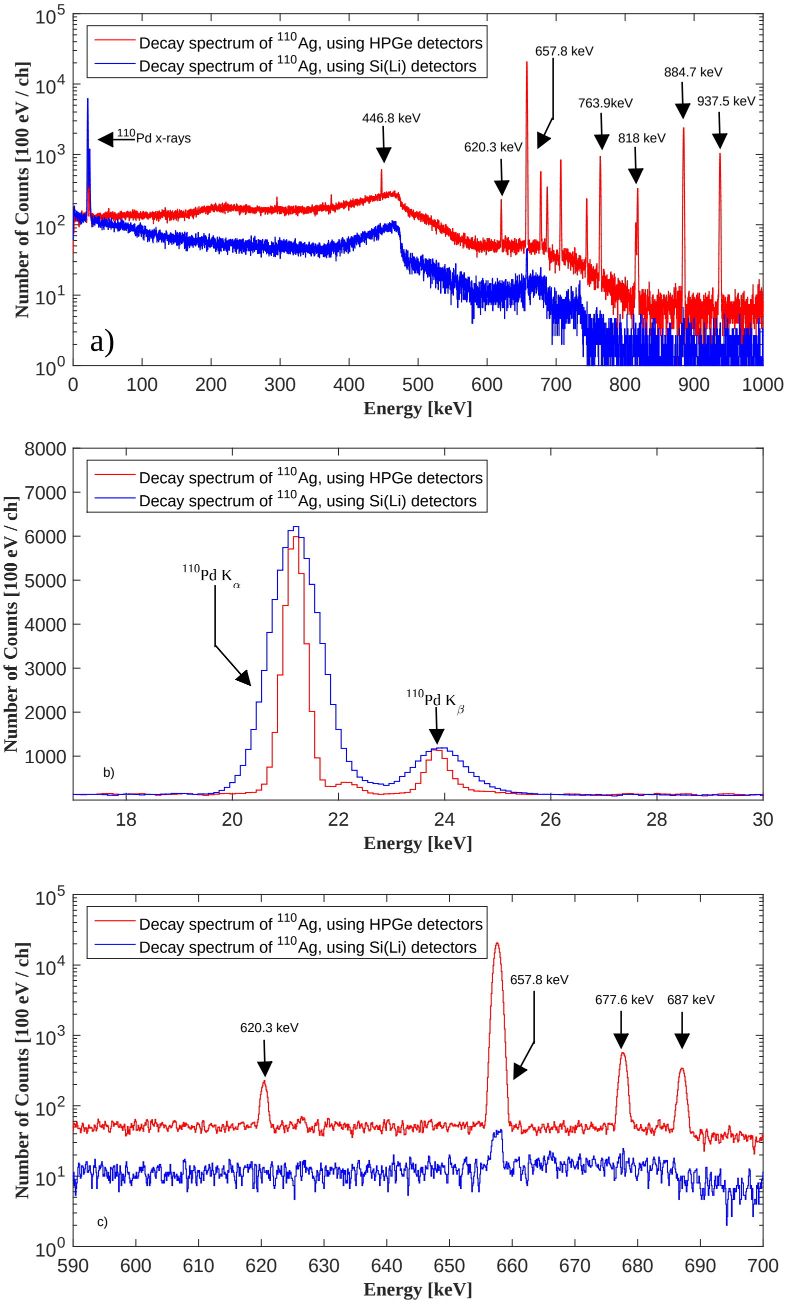

Figure 6.2: a) The top panel shows the comparison between simulated photon spectra from ^{110}Ag decay using 4 Si(Li) detectors (blue spectrum) in the 8 inch ports and 3 HPGe detectors (red spectrum) in 6 inch ports for future experiment using full trap geometry. The spectra show the nuclear transitions from ^{110}Ag decays based on 50 million events. b) Middle panel shows ^{110}Pd x-rays in energy range from 17 keV to 30 keV highlighting x-ray region. c) The bottom panel displays full γ energy deposition peaks in energy range from 590 keV to 700 keV, highlighting the differences in photon detection efficiencies in both detectors.

Bibliography

[1] D. Frekers, J. Dilling, and I. Tanihata. Electron capture branching ratios for the odd-odd intermediate nuclei in double-beta decay using the TITAN ion trap facility. *Canadian journal of physics*, 85(1):57–75, 2007.

[2] Ruben Saakyan. Two-Neutrino Double-Beta Decay. *Annual Review of Nuclear and Particle Science*, 63(1):503–529, October 2013.

[3] J. C. Bryan. *Introduction to nuclear science (3rd Edition)*. CRC Press, 2013.

[4] W. Bambynek, H. Behrens, M. H. Chen, B. Crasemann, M. L. Fitzpatrick, K. W. D. Ledingham, H. Genz, M. Mutterer, and R. L. Intemann. Orbital electron capture by the nucleus. *Reviews of Modern Physics*, 49(1):77, 1977.

[5] J. S. Welsh. Electron capture. *American journal of clinical oncology*, 29(6):540–542, 2006.

[6] B. Povh, M. Lavelle, K. Rith, C. Scholz, and F. Zetsche. *Particles and nuclei: an introduction to the physical concepts*. Springer, 2008.

[7] A. Lennarz, T. Brunner, C. Andreoiu, A. Chaudhuri, U. Chowdhury, P. Delheij, J. Dilling, S. Ettenauer, D. Frekers, A. T. Gallant, A. Grossheim, F. Jang, A. A. Kwiatkowski, T. Ma, E. Mané, M. R. Pearson, B. E. Schultz, M. C. Simon, and V. V. Simon. Electron-capture branching ratio measurements of odd-odd intermediate nuclei in double-beta decay at the TITAN facility. *Hyperfine Interactions*, 225(1-3):157–164, October 2013.

[8] M. Goeppert-Mayer. Double beta-disintegration. *Physical Review*, 48(6):512, 1935.

[9] C. F. V. Weizsäcker. Zur theorie der kernmassen. *Zeitschrift für Physik A Hadrons and Nuclei*, 96(7):431–458, 1935.

[10] T. Brunner. *In-trap decay spectroscopy for $\beta\beta$ decays*. PhD thesis, Technical University of Munich, 2011.

[11] A. Bohr and B. R. Mottelson. *Nuclear structure*, volume 1. World Scientific, 1998.

[12] V. A. Rodin, A. Faessler, F. Šimkovic, and P. Vogel. Assessment of uncertainties in qrpa $0\nu\beta\beta$-decay nuclear matrix elements. *Nuclear Physics A*, 766:107–131, 2006.

[13] W. H. Furry. On transition probabilities in double beta-disintegration. *Physical Review*, 56(12):1184, 1939.

[14] O. Civitarese and J. Suhonen. Light-neutrino mass spectrum, nuclear matrix elements, and the observability of neutrinoless $\beta\beta$ decay. *Nuclear Physics A*, 729(2):867–883, 2003.

[15] V. M. Gehman and S. R. Elliott. Multiple-isotope comparison for determining $0\nu\beta\beta$ mechanisms. *Journal of Physics G: Nuclear and Particle Physics*, 34(4):667, 2007.

[16] T. Otsuka, A. Arima, and F. Iachello. Nuclear shell model and interacting bosons. *Nuclear Physics A*, 309(1):1–33, 1978.

[17] J. Barea and F. Iachello. Neutrinoless double-β decay in the microscopic interacting boson model. *Physical Review C*, 79(4):044301, 2009.

[18] R. M. Eisberg and R. Resnick. *Quantum physics of atoms, molecules, solids, nuclei, and particles*. John Wiley & Sons, 1974.

[19] J. E. Turner. *Atoms, radiation, and radiation protection*. John Wiley & Sons, 2008.

[20] G. F. Knoll. *Radiation detection and measurement*. John Wiley & Sons, 2010.

[21] J. H. Hubbell. Photon mass attenuation and energy-absorption coefficients. *The International Journal of Applied Radiation and Isotopes*, 33(11):1269–1290, 1982.

[22] N. C. Lindquist, P. Nagpal, K. M. McPeak, D. J. Norris, and S. H. Oh. Engineering metallic nanostructures for plasmonics and nanophotonics. *Reports on progress in physics. Physical Society (Great Britain)*, 75(3):036501, 2012.

[23] G. Lutz. *Semiconductor Radiation Detectors: Device Physics*, volume 10. Springer Science & Business Media, 1999.

[24] C. Kittel and P. McEuen. *Introduction to solid state physics*, volume 8. John Wiley & Sons, 1976.

[25] T. I. Kamins. Hall Mobility in Chemically Deposited Polycrystalline Silicon. *Journal of Applied Physics*, 42(11):4357, December 1971.

[26] H. Spieler. *Semiconductor detector systems*. Oxford university press, 2005.

[27] P. Bricault, F. Ames, T. Achtzehn, M. Dombsky, F. Labrecque, J. Lassen, J. P. Lavoie, and N. Lecesne. An overview on TRIUMF's developments on ion source for radioactive beams. *Review of Scientific Instruments*, 79(2):02A908–02A908, 2008.

[28] TRIUMF. TRIUMF: Canadas National Laboratory for Particle and Nuclear Physics. http://www.triumf.ca/. Accessed: 2013.

[29] J. Dilling, R. Baartman, P. Bricault, M. Brodeur, L. Blomeley, F. Buchinger, J. Crawford, J.R. Crespo López-Urrutia, P. Delheij, M. Froese, G.P. Gwinner, Z. Ke, J.K.P. Lee, R.B. Moore, V. Ryjkov, G. Sikler, M. Smith, J. Ullrich, and J. Vaz. Mass measurements on highly charged radioactive ions, a new approach to high precision with TITAN. *International Journal of Mass Spectrometry*, 251(2-3):198–203, April 2006.

[30] M. Smith, L. Blomeley, P. Delheij, and J. Dilling. First tests of the TITAN digital RFQ beam cooler and buncher. *Hyperfine Interactions*, 173(1-3):171–180, 2006.

[31] T. Brunner, M.J. Smith, M. Brodeur, S. Ettenauer, A.T. Gallant, V.V. Simon, A. Chaudhuri, A. Lapierre, E. Mané, R. Ringle, M.C. Simon, J.A. Vaz, P. Delheij, M. Good, M.R. Pearson, and J. Dilling. TITAN's digital RFQ ion beam cooler and buncher, operation and performance. *Nuclear Instruments and Methods in Physics Research Section A: Accelerators, Spectrometers, Detectors and Associated Equipment*, 676:32–43, June 2012.

[32] M. Brodeur, V.L. Ryjkov, T. Brunner, S. Ettenauer, A.T. Gallant, V.V. Simon, M.J. Smith, A. Lapierre, R. Ringle, P. Delheij, M. Good, D. Lunney, and J. Dilling. Verifying the accuracy of the TITAN Penning-trap mass spectrometer. *International Journal of Mass Spectrometry*, 310:20–31, January 2012.

[33] A. Lapierre, M. Brodeur, T. Brunner, S. Ettenauer, A.T. Gallant, V. Simon, M. Good, M.W. Froese, J.R. Crespo López-Urrutia, P. Delheij, S. Epp, R. Ringle, S. Schwarz, J. Ullrich, and J. Dilling. The TITAN EBIT charge breeder for mass measurements on highly charged short-lived isotopesFirst online operation. *Nuclear Instruments and Methods in Physics Research Section A: Accelerators, Spectrometers, Detectors and Associated Equipment*, 624(1):54–64, December 2010.

[34] W. R. Plaß, T. Dickel, and C. Scheidenberger. Multiple-reflection time-of-flight mass spectrometry. *International Journal of Mass Spectrometry*, 349:134–144, 2013.

[35] A. Kellerbauer, T. Kim, R. B. Moore, and P. Varfalvy. Buffer gas cooling of ion beams. *Nuclear Instruments and Methods in Physics Research Section A: Accelerators, Spectrometers, Detectors and Associated Equipment*, 469(2):276–285, 2001.

[36] S. Sjue, D. Melconian, A. García, I. Ahmad, A. Algora, J. Äystö, V.-V. Elomaa, T. Eronen, J. Hakala, S. Hoedl, A. Kankainen, T. Kessler, I. Moore, F. Naab, H. Penttilä, S. Rahaman, A. Saastamoinen, H. Swanson, C. Weber, S. Triambak, and K. Deryckx. Electron-capture branch of Tc100 and tests of nuclear wave functions for double-β decays. *Physical Review C*, 78(6):064317, December 2008.

[37] A. Chaudhuri, C. Andreoiu, T. Brunner, U. Chowdhury, S. Ettenauer, D. Frekers, A.T. Gallant, A. Grossheim, G. Gwinner, R. Klawitter, A.A. Kwiatkowski, K.G. Leach, A. Lennarz, D. Lunney, T. D. Macdonald, B.E. Schultz, S. Seeraji, M.C. Simon, V.V. Simon, Dilling, and J. Precision mass measurements of short-lived nuclides for nuclear structure studies at TITAN. *EPJ Web of Conferences*, 66:02030, March 2014.

[38] G. Sikler, J. R. Crespo López-Urrutia, J. Dilling, S. Epp, C. J. Osborne, and J. Ullrich. A high-current EBIT for charge-breeding of radionuclides for the TITAN spectrometer. In *The 4th International Conference on Exotic Nuclei and Atomic Masses*, pages 63–64. Springer, 2005.

[39] R. Klawitter, M. Alanssari, U. Chowdhury, A. Chaudhuri, J. R. Crespo López-Urrutia, S. Ettenauer, A. T. Gallant, A. Grossheim, G. Gwinner, A. A. Kwiatkowski, K. Leach, A. Lennarz, T. D. Macdonald, M. C. Simon, B. E. Schultz, S. Seeraji, C. Andreoiu, D. Frekers, and J. Dilling. Progress at the TITAN-EBIT. In *Proceedings of the XII international symposium on electron beam ion sources and traps*, volume 1640, pages 112–119. AIP Publishing, January 2015.

[40] K.G. Leach, A. Grossheim, A. Lennarz, T. Brunner, J.R. Crespo López-Urrutia, A.T. Gallant, M. Good, R. Klawitter, A.A. Kwiatkowski, T. Ma, T.D. Macdonald, S. Seeraji, M.C. Simon, C. Andreoiu, J. Dilling, and D. Frekers. The TITAN in-trap decay spectroscopy facility at TRIUMF. *Nuclear Instruments and Methods in Physics Research Section A: Accelerators, Spectrometers, Detectors and Associated Equipment*, January 2015.

[41] J. Dilling, P. Bricault, M. Smith, and H-J. Kluge. The proposed TITAN facility at ISAC for very precise mass measurements on highly charged short-lived isotopes. *Nuclear Instruments and Methods in Physics Research Section B: Beam Interactions with Materials and Atoms*, 204:492–496, 2003.

[42] M. Brodeur. *First direct mass measurement of the two and four neutron halos ^{6}He and ^{8}He using the TITAN Penning trap mass spectrometer*. PhD thesis, University of British Columbia, 2009.

[43] K. G. Leach, A. Lennarz, A. Grossheim, C. Andreoiu, J. Dilling, D. Frekers, M. Good, and S. Seeraji. Sensitivity Increases for the TITAN Decay Spectroscopy Program. *arXiv preprint arXiv:1411.0026*, October 2014.

[44] S. Agostinelli, J. Allison, K. Amako, J. Apostolakis, H. Araujo, P. Arce, M. Asai, D. Axen, S. Banerjee, G. Barrand, F. Behner, L. Bellagamba, J. Boudreau, L. Broglia, A. Brunengo, H. Burkhardt, S. Chauvie, J. Chuma, R. Chytracek, G. Cooperman, G. Cosmo, P. Degtyarenko, A. Dell'Acqua, G. Depaola, D. Dietrich, R. Enami, A. Feliciello, C. Ferguson, H. Fesefeldt, G. Folger, F. Foppiano, A. Forti, S. Garelli, S. Giani, R. Giannitrapani, D. Gibin, J.J. Gómez Cadenas, I. González, G. Gracia Abril, G. Greeniaus, W. Greiner, V. Grichine, A. Grossheim, S. Guatelli, P. Gumplinger, R. Hamatsu, K. Hashimoto, H. Hasui, A. Heikkinen, A. Howard, V. Ivanchenko, A. Johnson, F.W. Jones, J. Kallenbach, N. Kanaya, M. Kawabata, Y. Kawabata, M. Kawaguti, S. Kelner, P. Kent, A. Kimura, T. Kodama, R. Kokoulin, M. Kossov, H. Kurashige, E. Lamanna, T. Lampén, V. Lara, V. Lefebure, F. Lei, M. Liendl, W. Lockman, F. Longo, S. Magni, M. Maire, E. Medernach, K. Minamimoto, P. Mora de Freitas, Y. Morita, K. Murakami, M. Nagamatu, R. Nartallo, P. Nieminen, T. Nishimura, K. Ohtsubo, M. Okamura, S. O'Neale, Y. Oohata, K. Paech, J. Perl, A. Pfeiffer, M.G. Pia, F. Ranjard, A. Rybin, S. Sadilov, E. Di Salvo, G. Santin, T. Sasaki, N. Savvas, Y. Sawada, S. Scherer, S. Sei,

V. Sirotenko, D. Smith, N. Starkov, H. Stoecker, J. Sulkimo, M. Takahata, S. Tanaka, E. Tcherniaev, E. Safai Tehrani, M. Tropeano, P. Truscott, H. Uno, L. Urban, P. Urban, M. Verderi, A. Walkden, W. Wander, H. Weber, J.P. Wellisch, T. Wenaus, D.C. Williams, D. Wright, T. Yamada, H. Yoshida, and D. Zschiesche. Geant4a simulation toolkit. *Nuclear Instruments and Methods in Physics Research Section A: Accelerators, Spectrometers, Detectors and Associated Equipment*, 506(3):250–303, July 2003.

[45] National Institute of Standards and Technology. The NIST reference on constants, units, and uncertainty. http://www.nist.gov/. Accessed: 2013.

[46] GEANT4: A toolkit for the simulation of the passage of particles through matter. http://geant4.cern.ch/. Accessed: 2013.

[47] R. C. Weast, M. J. Astle, and W. H. Beyer. *CRC handbook of chemistry and physics*, volume 69. CRC press Boca Raton, FL, 1988.

[48] E. Rand, J. Bangay, L. Bianco, R. Dunlop, P. Finlay, P. Garrett, K. G. Leach, A. Phillips, C. Svensson, C. Sumithrarachchi, and J. Wong. Geant4 simulations for the radon electric dipole moment search at TRIUMF. In *APS Division of Nuclear Physics Meeting Abstracts*, volume 1, 2010.

[49] Brookhaven National Laboratory. National Nuclear Data Center Interactive Chart of Nuclides. http://www.nndc.bnl.gov/chart/. Accessed: 2013.

[50] ROOT documentation. http://root.cern.ch/. Accessed: 2013.

[51] PENELOPE, A Code System for Monte-Carlo Simulation of Electron and Photon Transport. http://www.oecd-nea.org/. Accessed: 2013.

[52] K. G. Leach, A. Lennarz, A. Grossheim, R. Klawitter, T. Brunner, A. Chaudhuri, U. Chowdhury, J. R. Crespo López-Urrutia, A. T. Gallant, A. A. Kwiatkowski, T. D. Macdonald, B. E. Schultz, S. Seeraji, C. Andreoiu, D. Frekers, and J. Dilling. Low-Background In-Trap Decay Spectroscopy with TITAN at TRIUMF. *arXiv preprint arXiv:1411.4083*, November 2014.

[53] A. Lennarz, A. Grossheim, K.G. Leach, M. Alanssari, T. Brunner, A. Chaudhuri, U. Chowdhury, J.R. Crespo López-Urrutia, A.T. Gallant, M. Holl, A.A. Kwiatkowski, J. Lassen, T.D. Macdonald, B.E. Schultz, S. Seeraji, M.C. Simon, C. Andreoiu, J. Dilling, and D. Frekers. In-Trap Spectroscopy of Charge-Bred Radioactive Ions. *Physical Review Letters*, 113(8):082502, August 2014.

[54] P. Kunz, C. Andreoiu, P. Bricault, M. Dombsky, J. Lassen, A. Teigelhöfer, H. Heggen, and F. Wong. Nuclear and in-source laser spectroscopy with the ISAC yield station. *The Review of scientific instruments*, 85(5):053305, May 2014.

[55] T. Brunner, A. Lapierre, C. Andreoiu, M. Brodeur, P. Delheji, S. Ettenauer, D. Frekers, A. T. Gallant, R. Gernhäuser, A. Grossheim, R. Krücken, A. Lennarz, D. Lunney, D. Mücher, R. Ringle, M. C. Simon, V. V. Simon, S. K. L. Sjue, K. Zuber, and J. Dilling. Trapped-ion

decay spectroscopy towards the determination of ground-state components of double-beta decay matrix elements. *The European Physical Journal A*, 49(11):142, November 2013.

[56] L. Frevert and R. Schneberg. *Zeit. f. Phys*, volume 182. 1965.

[57] R. Keitel, D. Bishop, D. Dale, H. Hui, S. Kadantsev, M. Leross, R. Nussbaumer, J. Richards, E. Stuber, and G. Waters. Design and Commissioning of the ISAC Control System at TRIUMF. *ICALEPCS99, Trieste*, page 674, 1999.

[58] SIS3302-14xx Firmware-Gamma User Manual. http://www.struck.de. Accessed: 2013.

[59] S. Seeraji, C. Andreoiu, F. Jang, T. Ma, A. Chaudhuri, A. Grossheim, A. A. Kwiatkowski, B. E. Schultz, E. Mane, G. Gwinner, J. Dilling, A. Lennarz, D. Frekers, U. Chowdhury, V. V. Simon, T. Brunner, P. Delheij, and M. C. Simon. GEANT4 simulations for in trap decay spectroscopy for electron capture branching ratio measurements using the TITAN facility. In *APS Northwest Section Meeting Abstracts*, volume 1, 2012.

[60] J. Taylor. *Introduction to error analysis, the study of uncertainties in physical measurements*, volume 1. 1997.

Appendix A

Internal Drawing and Dimensions of Si(Li) Detector and Windows

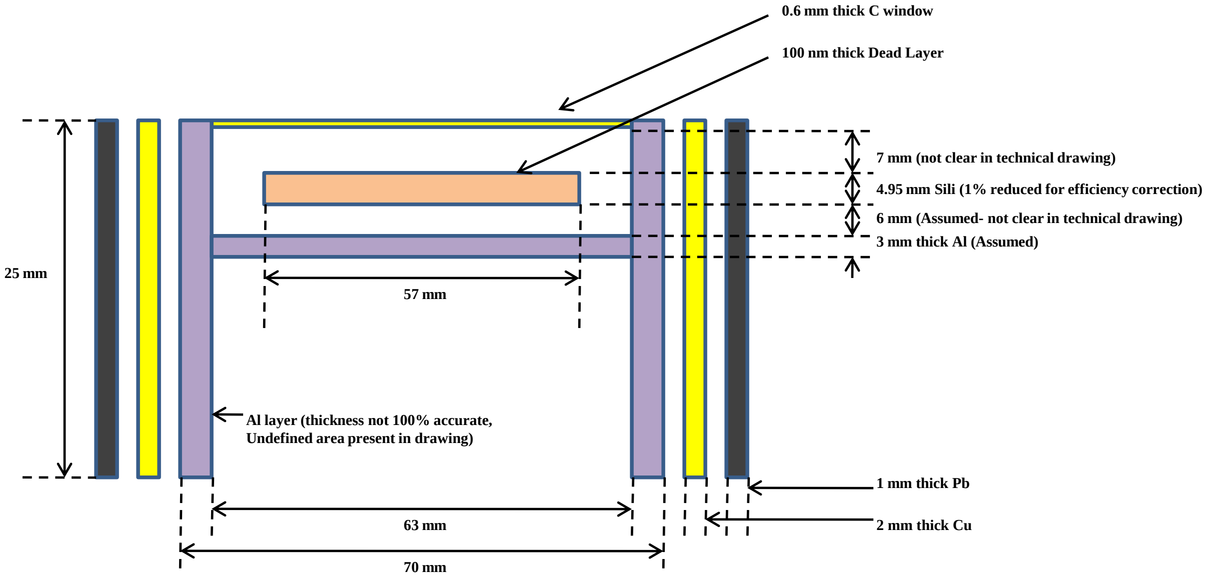

Figure A.1: Internal drawing and dimensions of the Si(Li) detector.

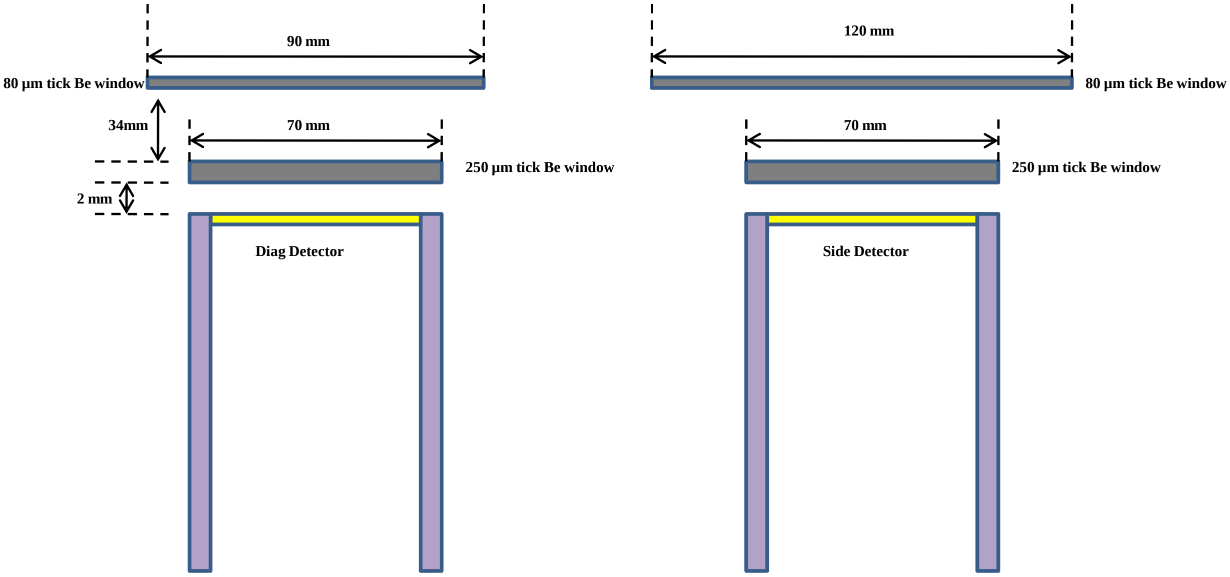

Figure A.2: Detailed dimensions of the (Be) windows.

Appendix B

Schematics of Pre-amplifier

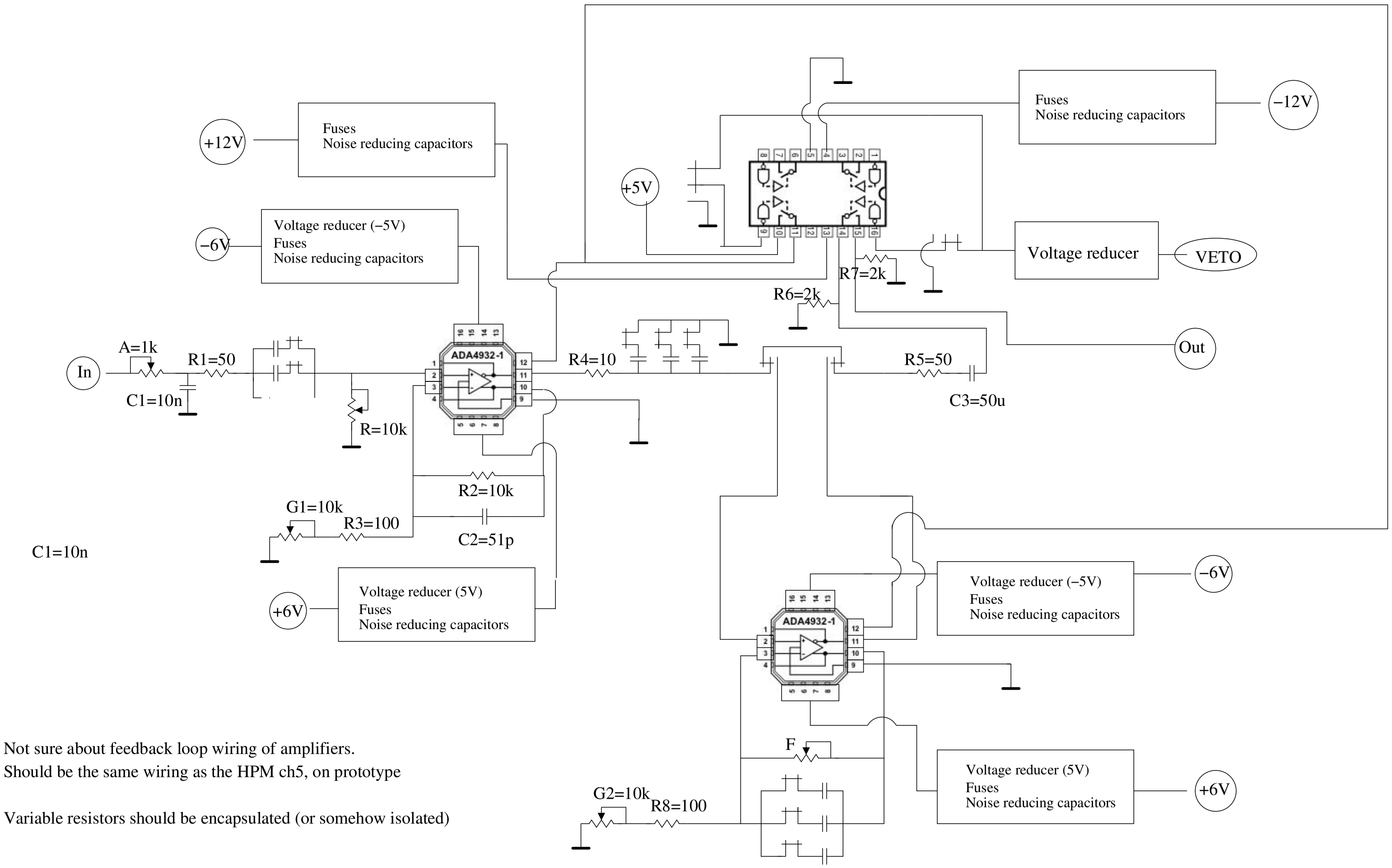

Not sure about feedback loop wiring of amplifiers.
Should be the same wiring as the HPM ch5, on prototype

Variable resistors should be encapsulated (or somehow isolated)

Figure B.1: Schematic diagram of pre-amplifier made by the SFU Electronic shop.

Appendix C

Input Files for GEANT4

Table C.1: Standard ^{133}Ba source input file for GEANT4 simulation

Source	Types of Particle	Number of Transition	Total Intensity	Type	Energy (keV)	NNDC Intensity
^{133}Ba						
	1					
		15				
			100			
				gamma	4.29	16.3
				gamma	30.625	35.1
				gamma	30.973	64.3
				gamma	34.92	6.09
				gamma	34.987	11.8
				gamma	35.818	3.64
				gamma	53.1525	2.199
				gamma	79.6139	2.62
				gamma	80.9977	34.1
				gamma	160.61089	0.645
				gamma	223.2373	0.45
				gamma	276.3997	7.164
				gamma	302.85	18.33
				gamma	356.0134	62.05
				gamma	383.848	8.4

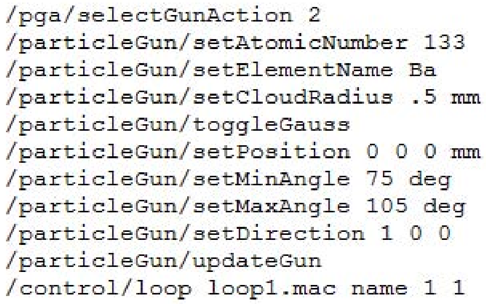

```
/pga/selectGunAction 2
/particleGun/setAtomicNumber 133
/particleGun/setElementName Ba
/particleGun/setCloudRadius .5 mm
/particleGun/toggleGauss
/particleGun/setPosition 0 0 0 mm
/particleGun/setMinAngle 75 deg
/particleGun/setMaxAngle 105 deg
/particleGun/setDirection 1 0 0
/particleGun/updateGun
/control/loop loop1.mac name 1 1
```

Figure C.1: A sample macro file to control the GEANT4 simulation.

Appendix D

Minimization for Scaling Data

Partial derivative needs to perform for minimizing $\chi^2 = \sum \left(\frac{y_i - \sum\limits_{k=1}^{m} a_k . f_k(x_i)}{\sigma_i^2} \right)^2$ with respect each parameters of a_k, take the partial derivative

$$\frac{\partial \chi^2}{\partial a_l} = -2 \sum \left[\frac{f_l(x_i)}{\sigma_i^2} \left[y_i - \sum_{k=1}^{m} a_k . f_k(x_i) \right] \right] = 0 \tag{D.1}$$

Thus, we obtain a set of m coupled equations for m parameters of a_l:

$$\sum y_i \frac{f_l(x_i)}{\sigma_i^2} = \sum_{k=l}^{m} \left[a_k \sum \left[\frac{1}{\sigma_i^2} f_l(x_i) f_k(x_i) \right] \right] \tag{D.2}$$

Equation D.2 can be expressed in matrix form

$$\beta = a . \alpha \tag{D.3}$$

The matrix β are defined by

$$\beta_k = \sum \left[\frac{1}{\sigma_i^2} y_i f_k(x_i) \right] \tag{D.4}$$

and the matrix α are defined by

$$\alpha_{lk} = \sum \left[\frac{1}{\sigma_i^2} f_l(x_i) f_k(x_i) \right] \tag{D.5}$$

Now the parameter matrix a can be obtained from equation D.3

$$a = \beta \alpha^{-} 1 \tag{D.6}$$

Appendix E

Decay Scheme

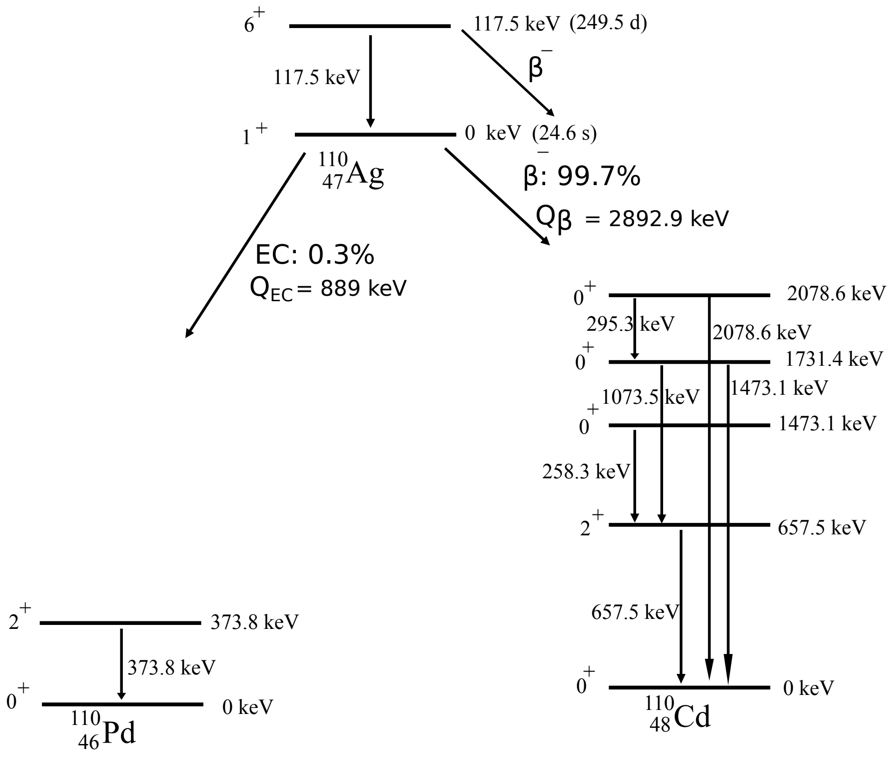

Figure E.1: Partial decay scheme of ^{110g,m}Ag.